

---

## Testing for the ‘predictability’ of dynamically triggered earthquakes in The Geysers geothermal field

Aiken Chastity<sup>1,2,\*</sup>, Meng Xiaofeng<sup>3,4,5</sup>, Hardebeck Jeanne<sup>6</sup>

<sup>1</sup> The University of Texas at Austin, Institute for Geophysics, Austin, TX, United States

<sup>2</sup> IFREMER, Marine Geosciences – LAD, Plouzané, France

<sup>3</sup> University of Washington, Department of Earth and Space Sciences, Seattle, WA, United States

<sup>4</sup> University of Washington, eScience Institute, Seattle, WA, United States

<sup>5</sup> Southern California Earthquake Center, University of Southern California, Los Angeles, CA, United States

<sup>6</sup> U.S. Geological Survey, Menlo Park, CA, United States

\* Corresponding author : Chastity Aiken, email address : [chastity.aiken@ifremer.fr](mailto:chastity.aiken@ifremer.fr)

---

### Abstract :

The Geysers geothermal field is well known for being susceptible to dynamic triggering of earthquakes by large distant earthquakes, owing to the introduction of fluids for energy production. Yet, it is unknown if dynamic triggering of earthquakes is ‘predictable’ or whether dynamic triggering could lead to a potential hazard for energy production. In this paper, our goal is to investigate the characteristics of triggering and the physical conditions that promote triggering to determine whether or not triggering is in anyway foreseeable. We find that, at present, triggering in The Geysers is not easily ‘predictable’ in terms of when and where based on observable physical conditions. However, triggered earthquake magnitude positively correlates with peak imparted dynamic stress, and larger dynamic stresses tend to trigger sequences similar to mainshock–aftershock sequences. Thus, we may be able to ‘predict’ what size earthquakes to expect at The Geysers following a large distant earthquake.

### Highlights

► Template matching event detection enhances statistical triggering test quality. ► Maximum triggered earthquake size positively correlates with dynamic stress. ► However, when and where triggering will occur is not easily ‘predictable’.

**Keywords :** dynamic triggering, template matching, earthquake, stress changes, The Geysers

## 60 **1. Introduction**

61           Passing seismic waves of large earthquakes can initiate seismic activity at remote  
62 distances either directly or indirectly, a phenomenon commonly known as dynamic triggering  
63 [*Hill and Prejean, 2015*]. Transient stresses on the order of a few kilopascals generated by large,  
64 distant earthquakes are known to dynamically trigger icequakes [*Peng et al., 2014*], deep tectonic  
65 tremor [e.g., *Aiken et al., 2013*], and shallow microearthquakes [e.g. *Hill et al., 1993*]. The  
66 general understanding is that triggered seismicity is “clock-advanced”, in that it occurs as a result  
67 of these small transient stresses loading an active fault and pushing it toward failure [e.g.,  
68 *Dietrich, 1994; Gomberg, 2010*]. Recent models of transient stress loading on active faults have  
69 indicated that triggering can be somewhat predictable, given certain information about the source  
70 of the stresses and information about the receiving fault [*Hill, 2012; Gonzalez-Huizar and*  
71 *Velasco, 2011*]. Thus, future earthquake rate increases due to transient stressing could possibly  
72 be predicted, if the conditions under which failure occurs are better understood [*Brodsky and van*  
73 *der Elst, 2014*].

74           Regions with high background activity are known to be most susceptible to dynamic  
75 triggering [*Hill and Prejean, 2015; Aiken and Peng, 2014*]. The Geysers geothermal field,  
76 located in northern California, is an extremely active fault system compared to other geothermal

77 areas in California. Even when considering only events with magnitude ( $M$ )  $\geq 2$ , The Geysers  
78 produced more earthquakes than other active geothermal fields in California combined over the  
79 last 15 years (Figure S1). In addition, large distant earthquakes have repeatedly triggered The  
80 Geysers [Prejean *et al.*, 2004; Brodsky, 2006; Aiken and Peng, 2014], making it a favorable  
81 region for exploring the characteristics of triggering and the conditions under which dynamic  
82 triggering of microearthquakes occurs.

83 In this study, we expand upon the systematic triggering analysis conducted by *Aiken and*  
84 *Peng* [2014]. In that work, small magnitude earthquakes ( $M < 4$ ) triggered in The Geysers were  
85 identified by visual inspection and compared to network-detected catalogs. Here, we apply the  
86 matched filter technique (Section 2) with the intention to further improve the catalog  
87 completeness for statistical tests. We search for key characteristics that could possibly explain  
88 the conditions that promote dynamic triggering of earthquakes, which include seismicity rates  
89 (Section 3), spatial extent and degree of triggering (Section 4), fault orientation dependence on  
90 triggering (Section 5), and The Geysers' stress state prior to mainshocks and during triggering  
91 (Section 6).

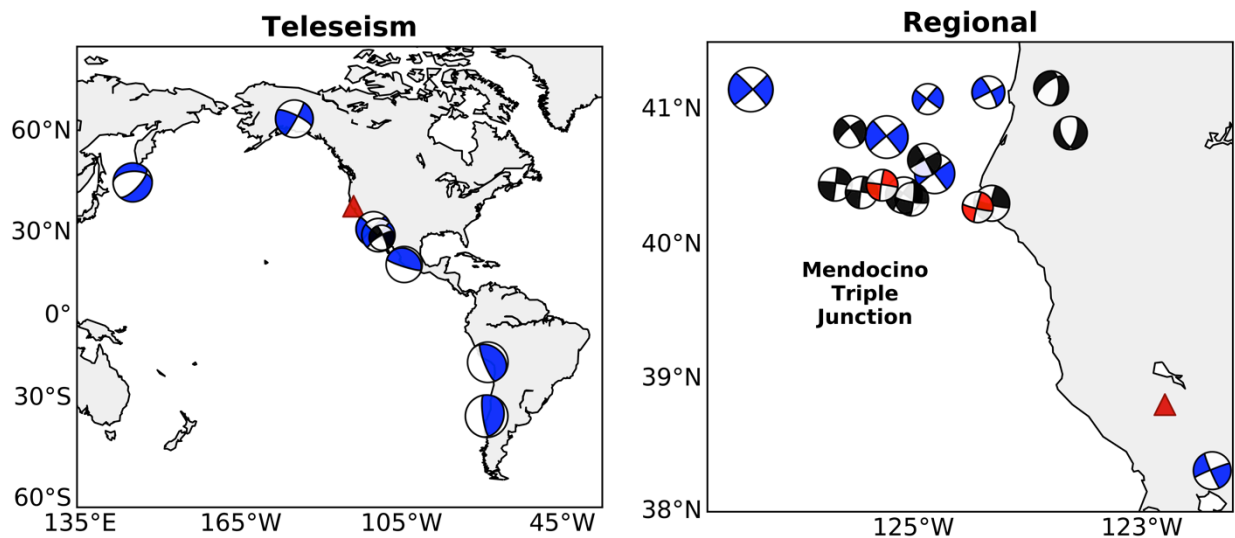
92

## 93 **2. Data and methods**

### 94 **2.1 Mainshock selection**

95 *Aiken and Peng* [2014] identified 10 large, distant mainshocks that triggered  
96 microearthquakes in The Geysers, based on statistically significant increased rate changes after  
97 the mainshocks. In each of those cases, microearthquakes ( $M < 4$ ) with  $S$ - $P$  time  $< 10$  seconds  
98 were hand-picked using 3-component waveform envelopes from a small number of stations.  
99 Here, we re-examine these same triggering mainshocks and also investigate triggering by 15

100 additional mainshocks. Namely, we select repeating  $M \geq 5$  earthquakes from offshore northern  
 101 California, which *Aiken and Peng* [2014] suggested to be a possible repeating dynamic triggering  
 102 source, and the August 24, 2014  $M6$  South Napa earthquake which occurred  $\sim 80$  km southeast of  
 103 The Geysers (Figure 1). Our study time period is limited to 2001 to early 2015. A complete list  
 104 of triggering sources (mainshocks) we investigate in this study can be found in Table 1, each of  
 105 which is reported in the Advanced National Seismic Systems (ANSS, a.k.a. ComCat) earthquake  
 106 catalog available from the Northern California Earthquake Data Center (NCEDC). Mainshocks  
 107 that are possibly repeat triggering sources from the Mendocino Triple Junction (MTJ) are listed  
 108 in Group 2 of Table 1; all other events are in Group 1.



109  
 110 **Figure 1.** Map illustrating focal mechanisms of triggering (blue) and non-triggering (black)  
 111 mainshocks (see Section 2) at teleseismic distances (left) and regional distances (right). Two  
 112 other non-triggering mainshocks in this study did not have reported focal mechanisms (red). We  
 113 assigned these two events mechanisms similar to their nearest neighbors. Size of the focal  
 114 mechanisms corresponds to magnitude (Table 1). The center of The Geysers seismicity is  
 115 marked by a red triangle.  
 116

**Table 1. Potentially triggering mainshocks investigated in this study.**

	Date	Time	Region*	$M^{**}$	Study
un p	06/23/2001	20:33:14	southern Peru	8.1	<i>Aiken and Peng</i> [2014]

	11/03/2002	22:12:42	Denali, AK	7.9	<i>Prejean et al. [2004]; Aiken and Peng [2014]</i>
	01/22/2003	02:06:35	Colima, MX	7.6	<i>Aiken and Peng [2014]</i>
	01/04/2006	08:32:32	Gulf of CA	6.6	<i>Aiken and Peng [2014]</i>
	01/13/2007	04:23:21	Kuril Islands	8.1	<i>Aiken and Peng [2014]</i>
	08/03/2009	17:59:56	Baja CA	6.9	<i>Aiken and Peng [2014]</i>
	04/04/2010	22:40:42	Baja CA	7.2	<i>Aiken and Peng [2014]</i>
	02/27/2010	06:34:12	Maule, Chile	8.8	<i>Aiken and Peng [2014]</i>
	08/24/2014	10:20:44	Napa, CA	6.0	This study
<b>Group 2</b>	09/20/2001	08:02:23	MTJ	5.1	This study
	06/17/2002	16:55:08	MTJ	5.2	This study
	08/15/2003	09:22:15	MTJ	5.3	This study
	06/15/2005	02:50:54	MTJ	7.2	<i>Brodsky [2006]; Aiken and Peng [2014]</i>
	07/19/2006	11:41:43	MTJ	5.0	This study
	02/26/2007	12:19:54	MTJ	5.4	This study
	05/09/2007	07:50:04	MTJ	5.2	This study
	06/25/2007	02:32:25	MTJ	5.0	This study
	04/30/2008	03:03:07	MTJ	5.4	This study
	01/10/2010	00:27:39	MTJ	6.5	<i>Aiken and Peng [2014]</i>
	02/04/2010	20:20:22	MTJ	5.9	This study
	02/13/2012	21:07:03	MTJ	5.6	<i>Aiken and Peng [2014]</i>
	07/21/2012	01:52:02	MTJ	5.1	This study
	03/10/2014	05:18:13	MTJ	6.8	<i>Aiken and Peng [2014]</i>
	01/01/2015	12:16:15	MTJ	5.3	This study
	01/28/2015	21:08:54	MTJ	5.7	This study

\*MTJ = Mendocino Triple Junction.

\*\*Magnitude as listed in the ANSS/ComCat catalog.

117

## 118 **2.2 Matched filter analysis**

119 We roughly follow the method of *Meng et al. [2013]* for detecting microearthquakes  
120 occurring in The Geysers around the times of each mainshock (Table 1) using the matched filter  
121 technique and briefly summarize our approach here. We utilize 17 seismic stations surrounding  
122 The Geysers (Table S1). For each station, we retrieve the vertical component continuous seismic  
123 waveforms half a day before to 1 day after each triggering mainshock from the NCEDC. This  
124 detection time is larger than that of *Aiken and Peng [2014]*, where microearthquakes occurring  $\pm$   
125 5 hours within the mainshock were identified by visual inspection. For each mainshock, we

126 select a total of 3,000 local earthquakes around its origin time from the ANSS/ComCat  
127 earthquake catalog and retrieve the vertical component seismic waveforms 0.5 seconds before  
128 and 3.5 seconds after each templates' *P*- or *S*-wave pick, whichever is available. These 3,000  
129 events are used as template events for scanning through continuous waveforms during the  
130 matched filter analysis. The time windows for selecting the template events from the NCEDC  
131 earthquake catalog can be found in Table S2.

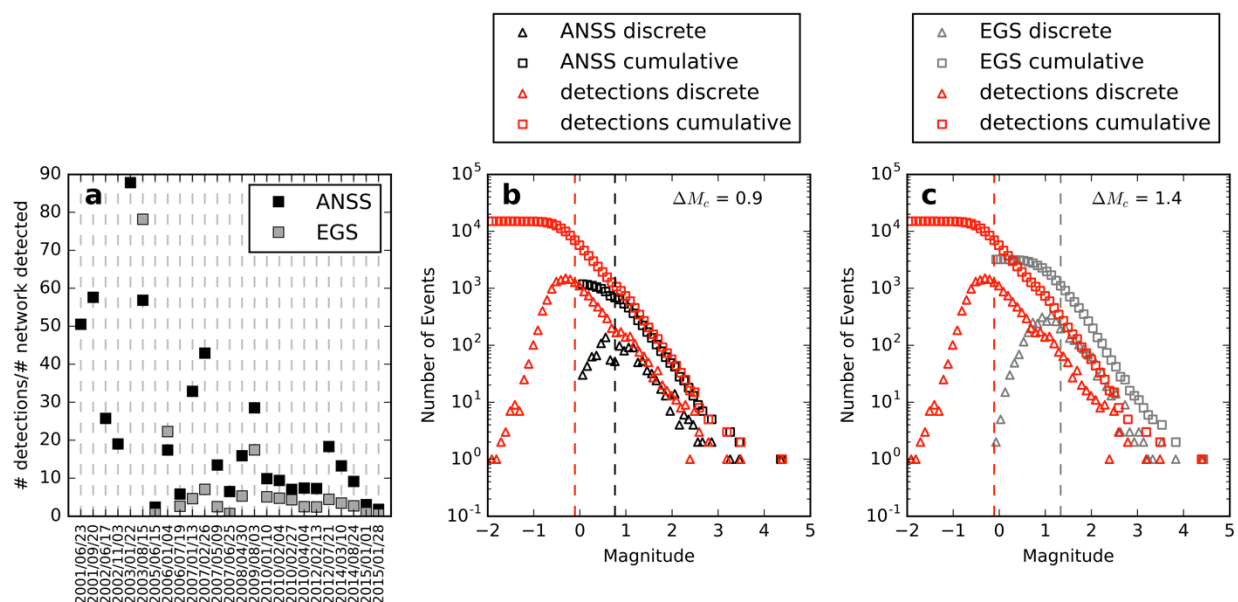
132 We next apply a 5 to 15 Hz band-pass filter to both continuous and template waveforms  
133 to enhance local earthquake signals and then down-sample the waveforms to 40 Hz to reduce  
134 computation time. On each channel, we compute the normalized cross-correlation between a  
135 single template and continuous waveforms at all data points, where the move-out of the template  
136 is fixed at each channel. Then, the correlation coefficients are shifted back by the negative of the  
137 move-out at each channel, and correlation traces from all channels are stacked into a mean cross-  
138 correlation trace, which increases the signal to noise ratio of small magnitude events. The event  
139 detection threshold is set as the sum of median value and 9 times the median absolute deviation  
140 from the mean correlation trace [e.g., *Shelly et al.*, 2007; *Peng and Zhao*, 2009; *Meng et al.*,  
141 2013]. With this detection threshold, we assign the hypocenters of detected events to be the same  
142 as that of the template. In doing so, the location uncertainty of the detected events is generally on  
143 the order of a few kilometers [Peng and Zhao, 2009]. Since we mainly focus on the temporal  
144 evolution of seismicity rate within the Geysers, the location uncertainty should not greatly affect  
145 our observations. We compute the magnitudes of detected events as follows:

$$146 \quad M_{detected} = M_{template} + \frac{1}{c} \log_{10} R \quad (1)$$

147 where  $M_{detected}$  and  $M_{template}$  is magnitude for the detected event and template, respectively,  $c$  is a  
148 constant, and  $R$  is the median peak amplitude ratio between the detected event and template

149 among all channels. Following previous studies [Peng and Zhao, 2009; Meng et al., 2013; Schaff  
 150 and Richards, 2014], we simply take the approximate  $c$  value as 1. We repeat this process for all  
 151 templates. When multiple templates detect the same event (i.e., origin times of detected events  
 152 have a separation time of less than 2 seconds), only the detection with the highest correlation  
 153 coefficient is kept.

154 With the matched filter analysis, we not only detect almost all events hand-picked by  
 155 Aiken and Peng [2014], but we also detect many more smaller local earthquakes (Figure S2).  
 156 Even though some hand-picked events made by Aiken and Peng [2014] are not detected by the  
 157 matched filter analysis (potentially bad analyst picks), overall the number of events detected  
 158 around the mainshocks increases (Figure 2a). We compared our detections to the ANSS/ComCat  
 159 catalog as well as the Enhanced Geothermal Systems (EGS) catalog reported by Lawrence  
 160 Berkeley National Laboratory and found that on average we improved the catalogs by  $\sim 20$  times.  
 161 In addition, the detection of many more small magnitude events reduces the magnitude of  
 162 completeness ( $M_c$ ) by  $\sim 1$  unit (Figure 2b-c) to  $-0.1$ .



164 **Figure 2.** Comparison between the combine ANSS and EGS catalogs and our detection catalogs.  
165 **(a)** Ratio of number detections made using matched filter to that reported in ANSS and EGS  
166 catalogs combined for each mainshock (see Section 2.1 in supplement for catalog combination).  
167 **(b)** Stacked Gutenberg-Richter distributions for detections made using matched filter and ANSS  
168 catalog. Black dashed line marks magnitude of completeness for ANSS ( $M_c = 0.8$ ) and red  
169 dashed line marks magnitude of completeness for stacked detection catalogs ( $M_c = -0.1$ ). **(c)**  
170 Same as (b) but for EGS catalogs. There is a noticeable difference between the magnitudes in the  
171 EGS and detection catalogs. This is because the magnitudes of the template events have  $M_d$   
172 magnitude while EGS reports  $M_L$  magnitudes. Overall, the magnitude of completeness is  
173 improved by  $\sim 1$  unit.  
174

### 175 **2.3 Focal mechanisms**

176 The focal mechanism of each template earthquake is found using first-motion polarities  
177 and take-off angles downloaded from the NCEDC and the program HASH [*Hardebeck and*  
178 *Shearer, 2002*]. We retained all mechanisms with quality A-C based on *Hardebeck and*  
179 *Shearer's* [2002] criteria, as well as those having  $\geq 10$  polarity observations and a mechanism  
180 misfit of  $< 0.2$  of the total polarities. We assign the focal mechanism of each newly-detected  
181 event to be the same as the template event it best matches, under the assumption that nearby  
182 events with similar waveforms are likely to have similar mechanisms. If a good-quality  
183 mechanism is not available for the best-fitting template, we use the next best fitting template  
184 with a mechanism. The focal mechanisms for the detections are approximately one-half strike-  
185 slip, one-third normal faulting, and the remaining one-sixth are distributed across a range of  
186 reverse and oblique orientations. The average of the strike-slip mechanisms is (strike= $166^\circ$ ,  
187 dip= $84^\circ$ , rake= $175^\circ$ ), and the average of the normal mechanisms is (strike= $19^\circ$ , dip= $45^\circ$ , rake= $-$   
188  $84^\circ$ ). These focal mechanisms are consistent with a NNE orientation of maximum horizontal  
189 stress, resulting in a normal and strike-slip faulting regime [*Boyle and Zoback, 2014*]. There may  
190 be missing events that have waveforms that are too dissimilar from any of the templates to meet  
191 the detection criteria, implying dissimilar focal mechanisms, and these mechanisms would be

192 unrepresented in the focal mechanism catalog. However, because the template matching  
193 detection method used in this study detects almost all of the events that *Aiken and Peng* [2014]  
194 identified by visual inspection using the waveform envelope, there are unlikely to be enough  
195 missing events to substantially affect the mechanism distribution. We note that we did not use  
196 events that *Aiken and Peng* [2014] identified by visual inspection in the template matching  
197 detection method or in focal mechanism analysis because there is no location information for  
198 those events.

199

### 200 **3. Rate changes around mainshocks**

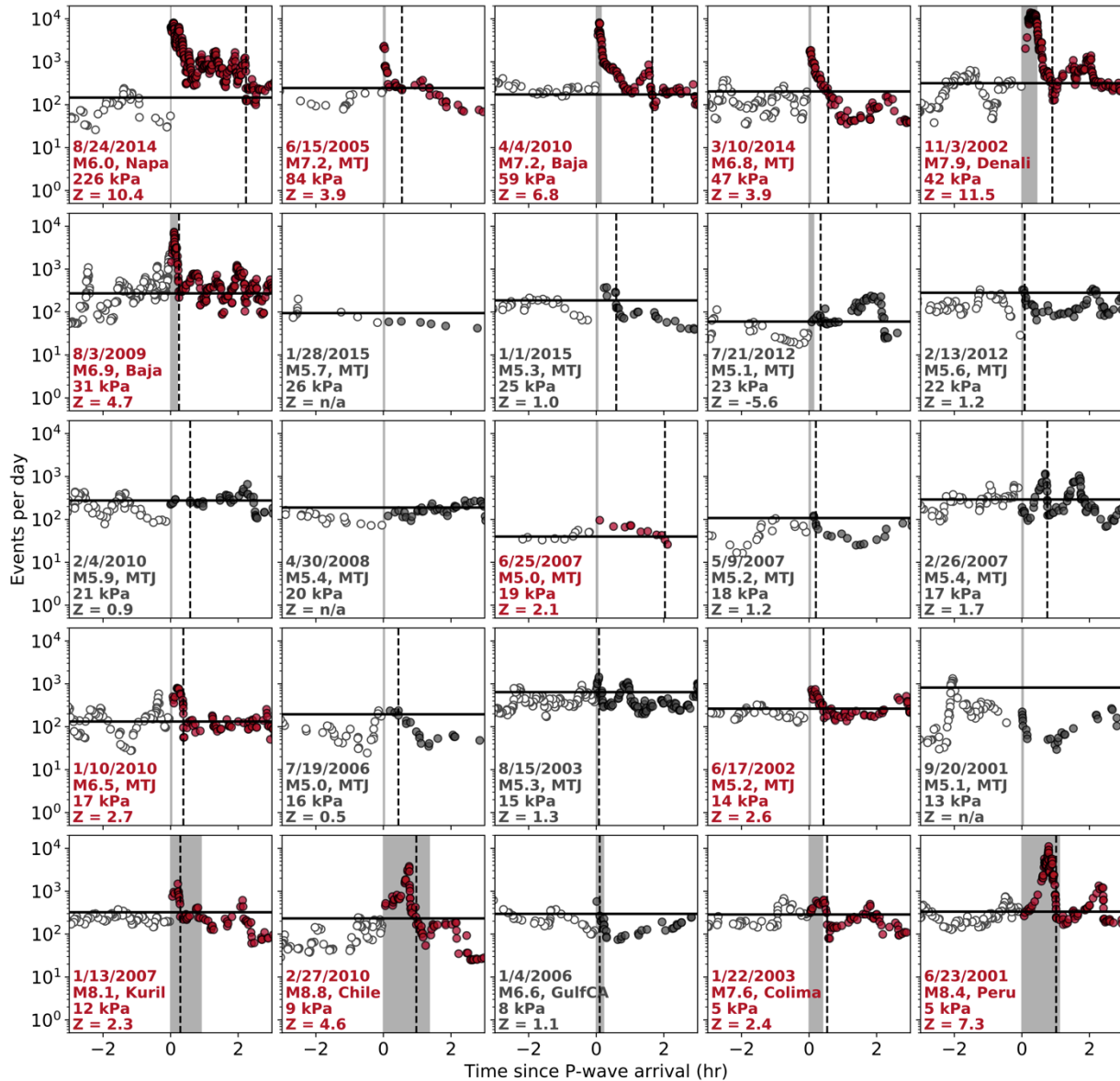
201         With the more complete catalogs formed using the matched filter method (Section 2.2),  
202 we can now better assess whether or not triggering occurred at The Geysers following each  
203 mainshock by determining if an increase in seismicity rate occurred. To do so, we compute the  
204 seismicity rates around the time of each mainshock by applying a sliding window approach on  
205 events in the detection catalogs [*Ziv et al.*, 2003; *Felzer and Brodsky*, 2006], using only events  
206 with  $M \geq M_c = -0.1$  (Section 2.2).

207         In some cases, the seismicity rates are elevated above the background rate in the first  
208 several hours following a mainshock. However, other mainshocks indicate no evidence of  
209 triggering even after detecting additional small magnitude events using the match filter method  
210 (Figure 3). For those mainshocks that have events occurring during the passing seismic waves or  
211 up to 30 minutes following a mainshock's  $2 \text{ km s}^{-1}$  surface wave arrival (to account for a slightly  
212 delayed triggering effect), we evaluate the significance of the rate change around the origin time  
213 of the triggering mainshocks by computing the  $Z$  value [*Habermann* 1981; *Habermann*, 1983].  
214 The  $Z$  value is a quantitative measure of the degree of triggering that compares the background

215 seismicity rate to the rate following a potential triggering mainshock. We use the  $Z$  value because  
216 it is a more symmetric version of the  $\beta$  value [Marsan and Wyss, 2011]. In general, when  $Z \geq$   
217 1.96 the seismicity rate increase is statistically significant at 95% confidence level:

$$218 \quad Z = \frac{N_a T_b - N_b T_a}{\sqrt{N_a T_b^2 + N_b T_a^2}} \quad (2)$$

219 where  $T_b$  and  $T_a$  are the background and triggering time windows, respectively. In our study, the  
220 background time window ( $T_b$ ) is the time of a mainshock's  $P$ -wave arrival plus 0.5 day before its  
221 origin time.  $N_b$  and  $N_a$  are the number of earthquakes in the background and triggering time  
222 windows, respectively.



223

224 **Figure 3.** Seismicity rates before (white) and after (red/black) each mainshock. Z values are  
 225 shown only for potential triggering earthquakes (i.e. distant mainshocks) with seismicity rates  
 226 above the background rate (solid black line) close to the time of the mainshock (see text for  
 227 details). Rates shown in red are for mainshocks with statistical significant rate increases ( $Z \geq$   
 228 1.96). Gray box = times when a mainshock's seismic waves pass through the region. Dashed line  
 229 = time at which the seismicity rate following the mainshock first falls below the background rate  
 230 threshold (solid black line) after the seismic waves began to pass through the region. Max  
 231 dynamic stress in kPa computed from measured peak ground velocities as in *Aiken and Peng*  
 232 [2014]. Mainshocks are organized top-down, left to right by decreasing dynamic stress.  
 233

234 In *Aiken and Peng* [2014], the triggering time window ( $T_a$ ) was limited to the time the  
235 surface waves imparted stress in the region, i.e. between the  $5 \text{ km s}^{-1}$  and  $2 \text{ km s}^{-1}$  wave arrivals.  
236 However, triggering can continue long after the surface waves have passed (Figure 3), and a  
237 triggering time window set for only during the surface waves of a mainshock will not account for  
238 events triggered by a cascading effect [*Brodsky, 2006*]. Therefore, in this study, we instead  
239 determine the length of the triggering time window ( $T_a$ ) by assessing when the elevated  
240 seismicity rate falls below a background rate. We note that in doing so we are maximizing the  $Z$   
241 value given all possible values of  $T_a$ . To determine  $T_a$ , we first estimate the background rate for  
242 each mainshock. Since the background seismicity rate can vary in time, we assume that the  
243 background rate is the median rate plus 1 times the median absolute deviation of the rates prior  
244 to the  $P$ -wave arrival of each mainshock. When the seismicity rate following a mainshock falls  
245 below the estimated background rate, we assume the triggering window has ended. The start of  
246 the triggering window, and thereby the end of the background window, for each mainshock is the  
247 arrival of its  $P$ -wave, as estimated using the iasp91 global velocity model in the *TauP* program  
248 (see Data and Resources). After determining the triggering time window length, we then count  
249 the number of events with  $M \geq M_c = -0.1$  occurring in the triggering time window and the  
250 background time window and compute the  $Z$  values for mainshocks with events during the  
251 passing seismic waves or up to 30 minutes following a mainshock's  $2 \text{ km s}^{-1}$  surface wave arrival.

252 While most cases of triggering are known in The Geysers [*Aiken and Peng, 2014*], the  
253 matched filter technique increased event detection and helped to delineate previously unclear  
254 triggering cases based on the computed  $Z$  values (Figure 3). For example, the 2007 Kuril Islands  
255 and the 2003 Colima mainshocks were considered to be 'possible' triggering mainshocks by  
256 *Aiken and Peng* [2014] because these mainshocks appeared to instantaneously trigger seismicity

257 with their passing seismic waves. However, *Aiken and Peng* [2014] used hand-picked events in  
258 their statistical test, which yielded  $Z < 1.96$ . From our matched filter analysis, we found that  
259 these mainshocks now have  $Z > 1.96$ , a sign that there was a significant increase in earthquake  
260 activity following these mainshocks. The 2006 Gulf of California earthquake was also  
261 considered to be a ‘possible’ triggering source by *Aiken and Peng* [2014] for the same reasons.  
262 However, contrary to previous cases, we determined that the rate change is low and no  
263 significant rate change was observed ( $Z = 1.3$ ). Finally, even though our choice of the triggering  
264 window length ( $T_a$ ) maximized the  $Z$  value for each mainshock, the  $T_a$  values did not disagree  
265 with easily recognizable triggering or non-triggering cases.

266 The seismicity rates for each mainshock in Figure 3 are ordered top-down left-to-right in  
267 order of decreasing dynamic stress ( $\sigma_d$ ), as computed from each mainshocks’ peak ground  
268 velocity (PGV) measured at the GDXB station of NC network and by assuming nominal values  
269 for shear rigidity ( $\gamma$ , 30 GPa) and phase velocity ( $v_{ph}$ , 3.5 km s<sup>-1</sup>) for the surface waves, i.e.  $\sigma_d = \gamma$   
270 \* PGV /  $v_{ph}$  [*Aiken and Peng*, 2014]. This expression approximates the maximum dynamic stress  
271 change recorded at the surface. Given that there is no site geology or classification for station  
272 GDXB (see Data Resources), we assume that the GDXB station is on hard rock. From Figure 3,  
273 it is clear that there are potentially two end-members of dynamic triggering - those mainshocks  
274 that generate large stress changes and those that generate small stress changes (i.e., mainshocks  
275 shown in red). In the next few sections, we explore in detail how these triggering cases are  
276 similar to and/or different from each other.

277

#### 278 **4. Spatial extent and degree of triggering**

279 Geothermal areas like The Geysers are thought to be in a constant state of critical stress  
280 due to on-going geothermal energy production and fluid circulation [*Hill and Prejean, 2015*].  
281 For a region that is in a constant state of critical stress, it is reasonable to assume that if  
282 triggering does occur that The Geysers will be activated in many areas by the passing seismic  
283 waves of a mainshock. This would be especially true if large dynamic stress acts on a critically  
284 stressed region since a greater dynamic stress has the potential to activate many more faults, i.e.  
285 fault patches that are further from failure. We test this theory by counting the number of  
286 triggered events during the triggering time window under the assumption that each triggered  
287 event represents a broken fault patch. We count broken fault patches (i.e. number of events  
288 triggered) for the 13 triggering mainshocks, excluding mainshocks that do not exhibit  
289 statistically significant triggering ( $Z < 1.96$ ) or have no computed  $Z$  values (Figure 3). We use  
290 the same triggering time windows as determined for each mainshock in Section 3.

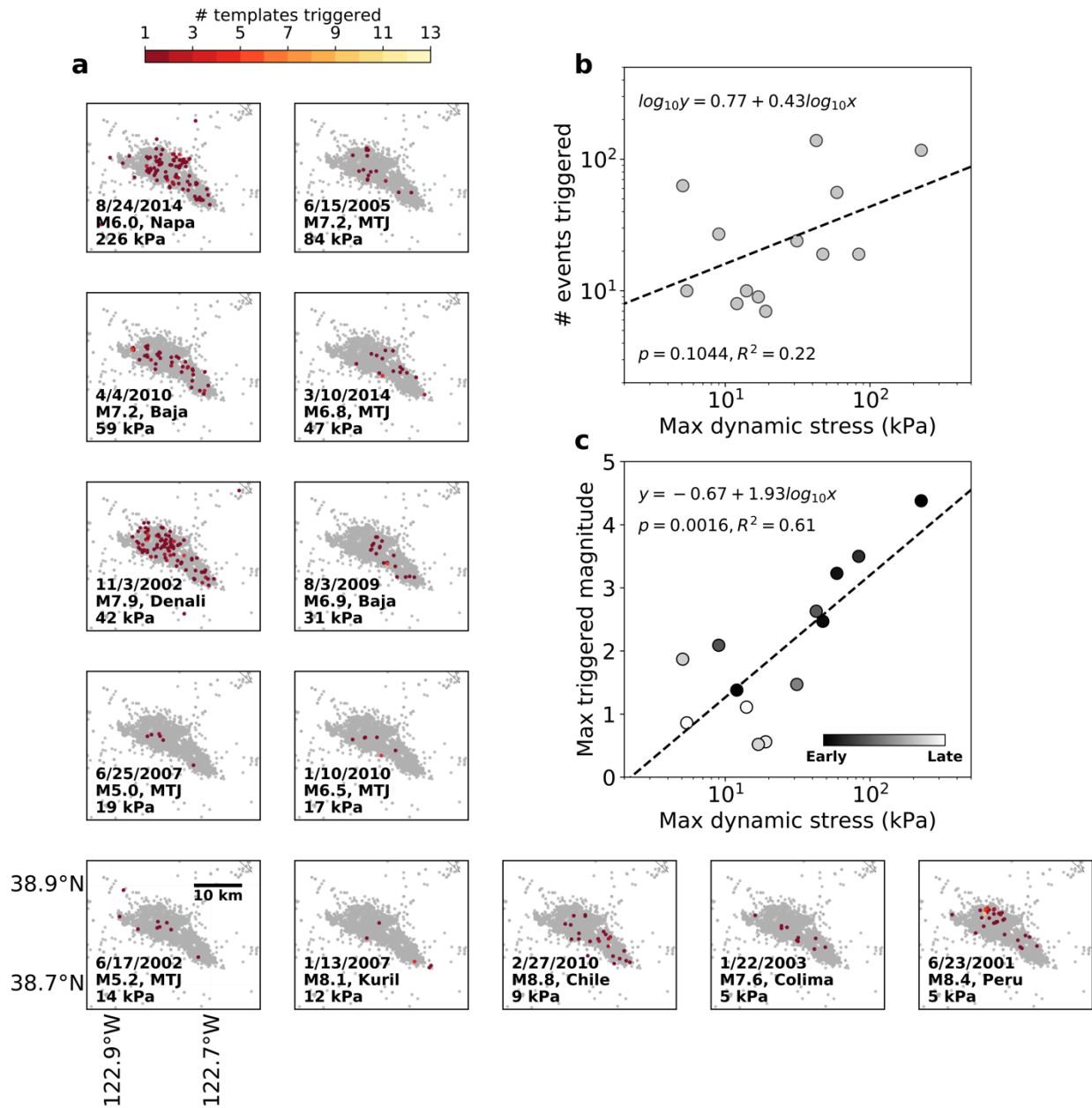
291 Figure 4a illustrates location of templates detected during the triggering time window for  
292 13 triggering mainshocks. While most mainshocks triggered small, localized areas, the 2014  
293 Napa and 2002 Denali mainshocks triggered most of The Geysers' seismically active area. In  
294 comparing the total number of triggered events to the maximum transferred dynamic stress of  
295 each mainshock (Figure 4b), we found no correlation. A lack of correlation between transferred  
296 dynamic stress and number of events triggered counters the argument of *Gomberg and Johnson*  
297 [2005], who suggested deformation at remote distances causes strain softening and a decrease in  
298 resistance to shear, which should ultimately lead to more failure (i.e. more broken fault patches).  
299 There are two possible explanations for our observation: 1) if fluid extraction is occurring at the  
300 time of triggering, then fault contact area and yield strength may increase or 2) triggering is  
301 happening, but asperities (fault patches) only partially slip, and the resulting seismic signal may

302 be of very small magnitude, i.e. undetectable. However, we do observe a positive correlation  
303 between the transferred dynamic stress and the maximum magnitude of triggered events (Figure  
304 4c). Mainshocks that transferred the most dynamic stress triggered larger events earlier in the  
305 triggering time window (Figure 4c), whereas mainshocks that transferred less dynamic stress  
306 triggered slightly smaller magnitude events occurring later in the triggered sequence.

307         Of course, these observations are based the quality of our matched filter detection  
308 catalogs. We utilized a detection threshold of 9 times the median absolute deviation (Section 2),  
309 which is typical for the matched filter analysis [e.g., *Shelly et al.*, 2007; *Peng and Zhao*, 2009;  
310 *Meng et al.*, 2013]. *Meng et al.*, [2013] found that local templates may falsely match regional  
311 earthquakes with correlation coefficients just above the threshold. To eliminate such false  
312 detections, one can expand the template library to cover a much larger area, which may increase  
313 the computation time by an order. Another way to eliminate false detections is to raise the  
314 detection threshold. The higher the detection threshold is, the lower the number of false  
315 detections will be. However, a higher threshold would also exclude many small local  
316 earthquakes that are buried within noises and significantly reduce the number of detected events.  
317 Therefore, we repeat the whole analysis with a moderately higher detection threshold of 12 times  
318 the median absolute deviation to evaluate the potential effects of false detections. Because the  
319 number of detected earthquakes significantly decreased, the statistical significance for a few  
320 triggering cases no longer exist. The number of significant triggering cases reduces from 13 to 7  
321 (Table S3). However, with the increased detection threshold, our observations remain the same  
322 (Figure S3), that is: 1) no correlation between the number of triggered events and maximum  
323 dynamic stress; 2) positive correlation between the dynamic stress and the maximum magnitude

324 of triggered events; 3) the higher the dynamic stress is, the earlier the maximum magnitude event  
 325 occurs in the sequence.

326



327

328 **Figure 4.** Maximum dynamic stress, number of triggered events, and maximum triggered  
 329 magnitude during triggering time windows for the 13 triggering mainshocks. **(a)** Mainshock date,  
 330 magnitude, location, and maximum dynamic stress are shown. MTJ = Mendocino Triple  
 331 Junction. All detections made in the region are shown as gray dots. There is no apparent  
 332 correlation between transferred dynamic stress and the area influenced, i.e. number of unique

333 templates. **(b)** There is a lack of significant correlation between number of events triggered and  
334 maximum dynamic stress transferred. **(c)** There is a significant positive correlation between  
335 maximum magnitude triggered, timing of the largest magnitude in the triggered sequence, and  
336 maximum dynamic stress transferred.  
337

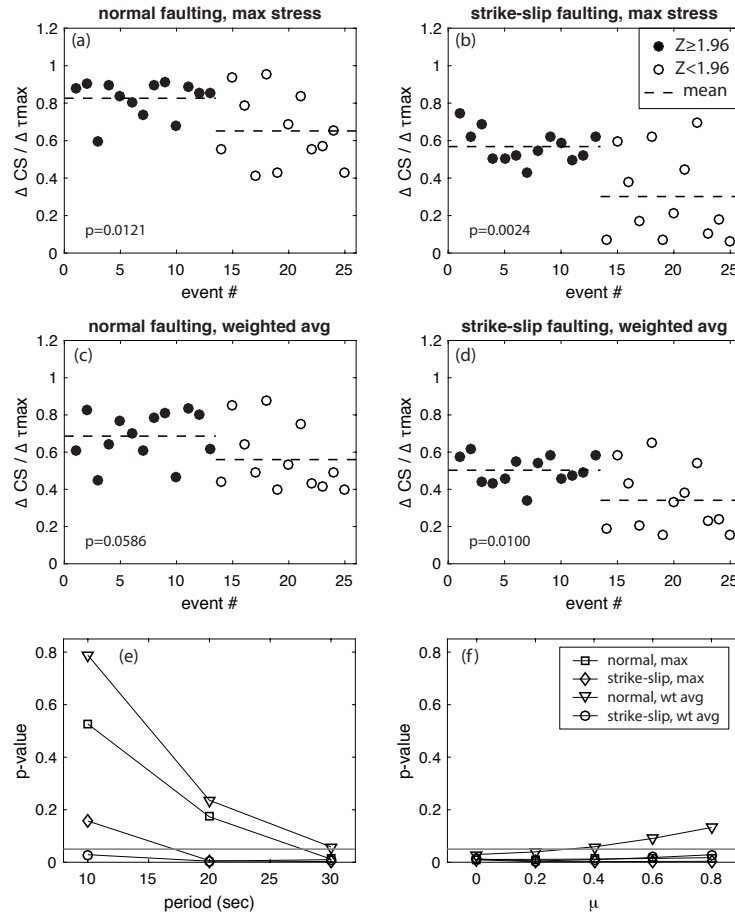
## 338 **5. Orientation dependence of triggering**

339         We next investigate whether the orientation of the dynamic stresses relative to the focal  
340 mechanisms encourages triggering at The Geysers. Previous sections explored the effects of  
341 absolute stress amplitude, and here we separately consider the effects of stress orientation. We  
342 look for systematic differences in dynamic stress orientations between triggering and non-  
343 triggering mainshocks, specifically the normalized dynamic Coulomb stress change resolved on  
344 typical Geysers' focal mechanisms (Section 2). The normalized Coulomb stress change measures  
345 the stress change on a given fault plane relative to the overall amplitude of the stress change,  
346 indicating how well oriented the dynamic stresses are for triggering that particular fault  
347 orientation. We define the normalized Coulomb stress change as  $\Delta CS/\Delta\tau_{max} = (\Delta\tau - \mu\Delta\sigma)/(\Delta\tau_{max})$ ,  
348 where  $\Delta\sigma$  is the normal stress change on the fault plane,  $\Delta\tau$  is the shear stress change in the rake  
349 direction, and  $\Delta\tau_{max}$  is the maximum shear stress change on a fault of any orientation (*i.e.* half the  
350 differential stress change). The apparent coefficient of friction,  $\mu$ , is varied from 0 to 0.8, and  
351 representative results for  $\mu = 0.4$  are shown. This is a typical value of apparent friction  
352 coefficient for Coulomb stress change [e.g., *King et al.*, 1994]

353         We compute the dynamic strain tensor as a function of time for each mainshock in Table  
354 1 using the Direct Greens Function code of *Pollitz* [1996], for periods of  $\geq 8$  s, low-pass filter at  
355 10 s, 20 s, or 30 s, and convert to stress by assuming a shear modulus of 30 GPa. The stress is  
356 computed at 5 km depth to approximate the shallow depths of the earthquakes. We consider two  
357 representative focal mechanisms as determined in Section 2.3, one normal and one strike-slip,

358 with (strike, dip, rake) of (20°, 45°, -90°) and (170°, 90°, 180°) and take the largest stress change  
359 on either nodal plane of each mechanism. We find the normalized Coulomb stress change at the  
360 time of the largest differential stress change, and a weighted average Coulomb stress change over  
361 the whole time series to capture more of the high-amplitude stress changes.

362 At longer periods (low-pass at 30 s), the normalized Coulomb stress changes tend to be  
363 visibly higher on average for the mainshocks with significant triggering ( $Z \geq 1.96$ ) than for those  
364 without significant triggering ( $Z < 1.96$ ) (Figure 5a-d). This holds when we consider the  
365 maximum stress changes on representative normal and strike-slip faults and the weighted  
366 average stress change on the representative normal and strike-slip faults. A Student's t-test  
367 confirms that we can reject the null hypothesis that the results for the events with  $Z \geq 1.96$  and  $Z$   
368  $< 1.96$  have the same mean with  $\geq 95\%$  confidence, except for the case of the weighted average  
369 stress for normal faults. For a low-pass filter at 20 s, the difference is significant only for the  
370 strike-slip mechanism, and for a low-pass filter at 10 s, it is only significant for the case of the  
371 weighted average for strike-slip faults (Figure 5e). Overall, the results are not highly sensitive to  
372 the value of  $\mu$  (Figure 5f). The stronger correlation with triggering at longer periods is consistent  
373 with the results of *Hardebeck* [2014] for near-field dynamic triggering and suggests that surface  
374 waves are responsible for triggering. Moreover, based on The Geysers' dominant faulting  
375 orientations and fault orientation of the potentially triggering mainshocks, surface waves tend to  
376 be close to or at their greatest triggering potential for triggering mainshocks as opposed to non-  
377 triggering mainshocks [*Hill*, 2012](Figure 6). The results imply that mainshocks are more likely  
378 to trigger seismicity at The Geysers if the long-period dynamic stresses are well oriented to load  
379 the typical Geysers' focal mechanisms with increased Coulomb stress.



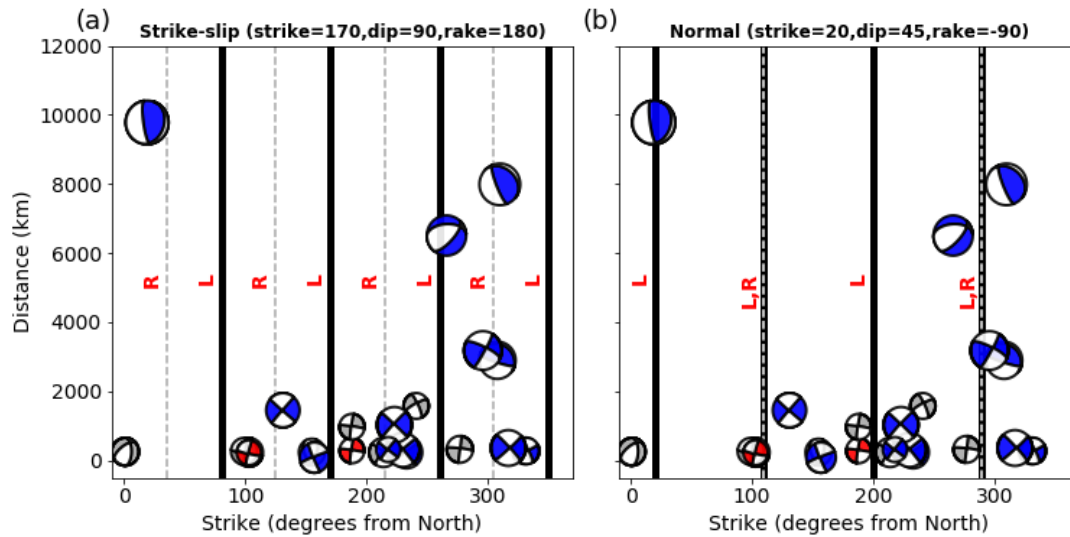
380

381 **Figure 5.** (a) Normalized Coulomb stress change at the time of the largest differential stress  
 382 change, resolved on typical Geysers' normal faulting orientation of strike= $20^\circ$ , dip= $45^\circ$ , rake= $-$   
 383  $90^\circ$ , for synthetic stressgrams low-passed at 30s. The triggering (filled circles) and non-  
 384 triggering (open circles) mainshocks are shown, along with the mean of each (dashed line). The  
 385  $p$ -values are for a Student's  $t$ -test of the null hypothesis that the results for the triggering and  
 386 non-triggering mainshocks have the same mean. (b) Normalized Coulomb stress change at the  
 387 time of the largest differential stress change, projected on a typical strike-slip orientation of  
 388 strike= $170^\circ$ , dip= $90^\circ$ , rake= $180^\circ$ . (c) Weighted average normalized Coulomb stress change,  
 389 projected on the typical normal faulting orientation. (d) Weighted average normalized Coulomb  
 390 stress change, projected on the typical strike-slip orientation. (e) The  $p$ -value for the Student's  $t$ -  
 391 test of the null hypothesis that the results for the triggering and non-triggering mainshocks have  
 392 the same mean, as a function of the period of the low-pass filter applied to the synthetic  
 393 stressgrams. (f) The  $p$ -value for the Student's  $t$ -test of the null hypothesis, as a function of the  
 394 assumed apparent coefficient of friction,  $\mu$ .

395

396

397



398

399 **Figure 6.** Approximate maximum triggering potential of surface waves from triggering  
 400 mainshocks (blue) and non-triggering mainshocks (gray/red) on a (a) strike-slip and (b)  
 401 normal fault in The Geysers. The red focal mechanisms are estimated based on their nearest neighbor  
 402 (see Figure 1). Solid black lines represent approximate greatest triggering potential for Love  
 403 waves (L). Dashed gray line represents approximate greatest triggering potential for Rayleigh  
 404 waves (R). For a normal fault, Love wave maximum triggering potential incidence is similar to a  
 405 strike-slip fault, but the potential for a Love wave to trigger decreases as fault dip departs from  
 406 vertical [Hill, 2012].

407

408 *Hardebeck* [2014] showed that aftershocks in a non-geothermal setting had a different  
 409 distribution of focal mechanisms than the earthquakes occurring before the mainshock. The  
 410 aftershock rake directions were better aligned with the dynamic shear stresses resolved on the  
 411 fault planes, demonstrating that triggering was linked to the orientation of the dynamic stresses.  
 412 We search for a similar change in focal mechanisms for the triggered events at The Geysers. We  
 413 characterize the population of focal mechanisms before and after each mainshock as a joint  
 414 probability distribution function,  $P(\theta, \varphi, \lambda)$ , of the trend and plunge ( $\theta, \varphi$ ) of the normal to the  
 415 nodal plane, and the corresponding rake,  $\lambda$ . Both nodal planes are included due to the nodal  
 416 plane ambiguity. We look for significant changes in the focal mechanism distribution by  
 417 considering  $\Delta P(\theta, \varphi, \lambda) = P_{post}(\theta, \varphi, \lambda) - P_{pre}(\theta, \varphi, \lambda)$ . Some non-zero values of  $\Delta P$  will occur simply

418 due to chance, even if there is no true change in the underlying distribution, due to errors or  
419 unrelated fluctuations in the focal mechanism catalog. We characterize the expected distribution  
420 of  $|\Delta P|$  due to chance by randomly reshuffling the pre- and post-mainshock events.

421 We find that the observed distribution of  $|\Delta P|$  generally falls within the middle 95% of  
422 1000 realizations of the reshuffled catalogs. Therefore, we consider any changes in the observed  
423 mechanism distribution to be due to chance and not reflecting significant changes in the  
424 underlying focal mechanism distribution (Figure S4). This holds true for each mainshock  
425 individually, as well as for a stack of all mainshocks and a stack of only those mainshocks where  
426 the triggering is found to be significant ( $Z \geq 1.96$ ). To investigate whether a signal may be  
427 obscured because the detection threshold is too low to ensure that a detected event and its  
428 template have similar focal mechanisms, we try a higher cross-correlation threshold (0.5) and do  
429 not find the changes to be significant. Finally, we consider only the first 2 hours of post-  
430 mainshock events (there are too few events with mechanisms to limit the analysis to the  
431 triggering window), and again do not find the focal mechanism changes to be significant.  
432 Comparatively, the plunge of injection-induced earthquakes has been shown to change during  
433 times of peak-injection rates but return nearly to before injection plunge after injection rates fall  
434 [*Martinez-Garzon et al.*, 2013]. These observations suggest that dynamic stress changes could  
435 pressurize fluids in the crust, but that these stress changes are not localized, quasi-static stress  
436 changes like that caused by fluid injection. That is to say, the dynamic stress changes from  
437 distant mainshocks do not appear to alter the stress field, at least in dynamic triggering time  
438 scales.

439

440 **6. Stress dependence on triggering**

## 441 6.1 Localized stress changes

442 One factor that could play a role in whether or not triggering occurs is a region's stress  
443 state prior to the arrival of a mainshock's seismic waves. Recent laboratory experiments and  
444 seismicity studies have shown that the  $b$  value of the Gutenberg-Richter equation can possibly be  
445 used to approximate the stress state on a fault [Schorlemmer and Wiemer, 2005; Göebel et al.,  
446 2013; Tormann et al., 2014]. Therefore, the  $b$  value, which describes the size distribution of  
447 earthquakes, can possibly act as a 'stressmeter', when the stress state of a region cannot be  
448 measured directly [Aki, 1965]. In the case of The Geysers, we assess the stress state prior to each  
449 mainshock by computing the  $b$  value using the maximum likelihood method [Aki, 1965;  
450 Marzocchi and Sandri, 2003]:

$$451 \quad b = \frac{1}{\ln(10)[M_{avg} - (M_{thresh} - \Delta M / 2)]} \quad (3)$$

452 where we set  $M_{thresh}$  to be  $M_c$  (magnitude of completeness),  $M_{avg}$  is the average magnitude of all  
453 events above  $M_{thresh}$  and  $\Delta M$  is magnitude binning size (typically 0.1). There are many methods  
454 for computing the  $M_c$  of a catalog. In our study, we simply use the maximum curvature method  
455 [Wiemer and Wyss, 2000] and add 0.2 units. Adding 0.2 units is considered a more accurate  
456 representation of  $M_c$  when using the maximum curvature method because it provides a similar  
457 result to the entire magnitude range method [Mignan and Woessner, 2012].

458 Since earthquake activity varies in space, the  $b$  value will also vary in space. To evaluate  
459 the  $b$  value as a 'stressmeter', we investigate the  $b$  value prior to mainshocks in areas that are  
460 triggered and not triggered. We create nodes with  $0.01^\circ \times 0.01^\circ$  spacing for The Geysers  
461 (longitude min/max:  $123^\circ\text{W}$ ,  $122.6^\circ\text{W}$ ; latitude min/max:  $38.6^\circ\text{N}$ ,  $39^\circ\text{N}$ ). For each node, we  
462 select earthquakes within a cylinder centered at the node with a radius equal to the greatest  
463 distance to the nearest 8 nodes. For example,  $0.01^\circ \times 0.01^\circ$  spacing would have a cylinder radius

464 of  $[(1.1 \text{ km})^2 + (1.1 \text{ km})^2]^{1/2} \approx 1.6 \text{ km}$ . We do not regard depth as a factor in our  $b$ -value  
465 calculation because most events occur at depths less than 5 km. At each node, we sample 2,000  
466 earthquakes occurring in a cylinder prior to each potential triggering mainshock time to obtain an  
467 adequate number of events above the magnitude of completeness ( $M_c$ ). We compute the  $M_c$  and  
468 then the  $b$  value at each node according to equation (3) if there are at least 500 events above the  
469  $M_c$ , which guarantees smaller  $b$  value error [Nava, 2017]. We note that there are no set time  
470 frames for events sampled in the cylinder about a node and that only the last 2000-events  
471 occurring before the each potential triggering mainshock time are selected for the calculation.  
472 When set time frames were used, in most cases, we found that we did not have enough events to  
473 obtain a stable  $b$  value for a node.

474 For this calculation, we combine ANSS/ComCat and EGS catalogs from January 2000 to  
475 January 2016, removing duplicate events ( $< 1$  second apart and  $< 1$  km apart). For events in The  
476 Geysers during our study time period, the ANSS/ComCat catalog reported mostly duration  
477 magnitude ( $M_d$ ) while the EGS catalog reported local magnitudes ( $M_L$ ). The magnitude  
478 differences for duplicate events in our combined ANSS and EGS catalogs is typically  $\sim 0.7$  units  
479 (Figure S5). Since  $b$  value is dependent upon magnitudes sampled, we adjust event magnitudes  
480 in the EGS catalog to be comparable to the ANSS/ComCat reported magnitudes by  $M_{ANSS} = M_{EGS}$   
481  $- 0.66$  before our  $b$  value analysis (for more details see supplementary material). This magnitude  
482 adjustment is similar to Hawkins *et al.* [2017]. We use the combined, magnitude-adjusted  
483 catalogs for the  $b$  value calculation because our matched filter detections were made up to 12  
484 hours prior to the mainshocks, and in most cases, there were not enough detections for an  
485 adequate frequency-magnitude distribution.

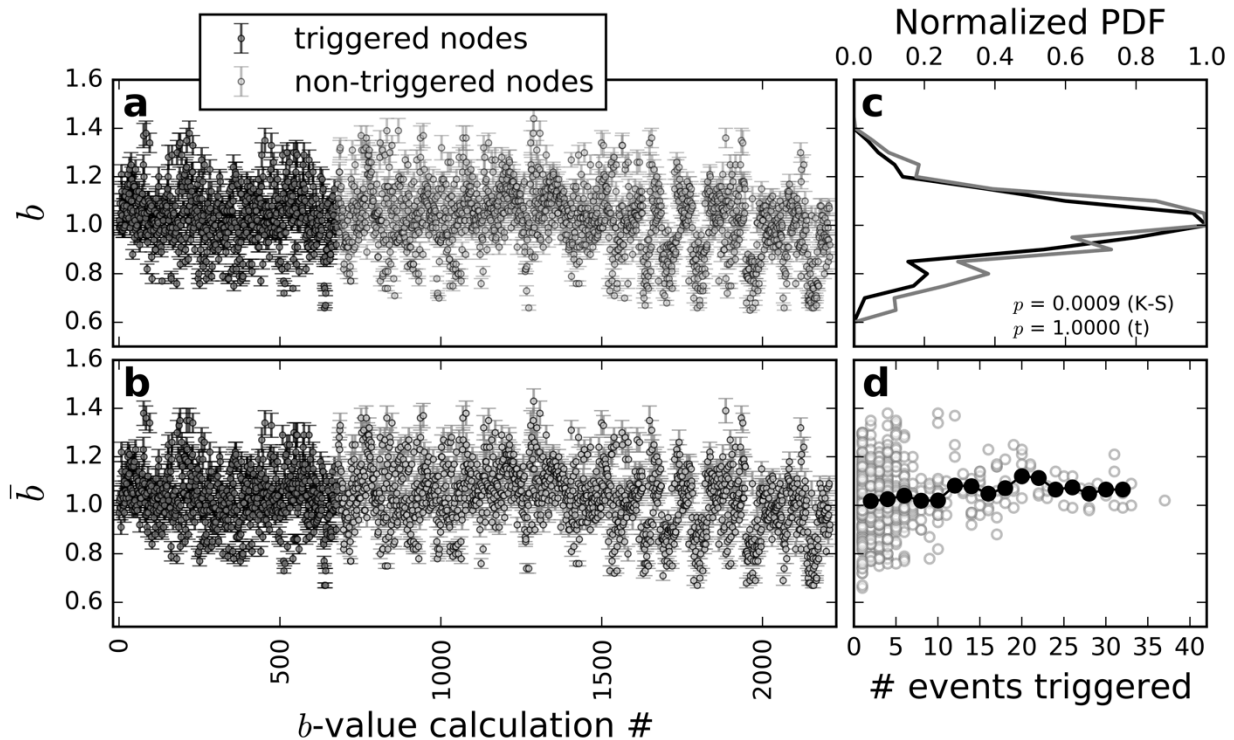
486 We compute  $b$  values as described above for each mainshock and for each node,  
487 differentiating between triggered and non-triggered nodes. A triggered node is defined as simply  
488 a cylinder about the node point that contains at least one event in the triggering time window  
489 following a mainshock that exhibits statistical significance, i.e.  $Z > 1.96$  (Section 3). In addition,  
490 we assess the uncertainty in our  $b$  value calculations via bootstrapping [*Schorlemmer et al.*, 2003]  
491 and with  $b$  value error. The  $b$  value error, as provided by *Shi and Bolt* [1982], is:

$$492 \quad \sigma_b^{SB} = 2.3b^2 \sqrt{\frac{\sum_{i=1}^N (M_i - M_{avg})^2}{N(N-1)}}. \quad (4)$$

493 At each node, we construct 100 random samplings with replacement from the true 2,000-event  
494 set at that node and compute the mean  $b$  value and mean error across the samplings, as described  
495 in equations (3) and (4). The  $b$  values computed from randomly sampled earthquakes exhibit  
496 minor differences from both the true triggered and non-triggered  $b$  value distributions,  
497 evidencing that our true  $b$  values are stable (Figure 7a-b). A Kolmogorov–Smirnov test for  
498 similarity between the true triggered and non-triggered node  $b$  value distributions yields a  $p$ -  
499 value = 0.0009, which suggests that the distributions are different. However, a Student’s t-test  
500 provides a  $p$ -value = 1. Taken together, this illustrates that the means of the true triggered and  
501 non-triggered node  $b$  value distributions are similar (t-test:  $p = 1$ ), but their standard deviations  
502 are slightly different (Figure 7c). Thus,  $b$  value distributions at triggered nodes are not  
503 distinguishable from those at non-triggered nodes. In addition, when comparing the number of  
504 events triggered in a node to the  $b$  value computed at that node, there is no direct evidence that a  
505 node with a smaller  $b$  value (indication of a region with higher differential stress) is susceptible  
506 to having more earthquakes triggered (Figure 7d). These observations hold when node sample  
507 spacing is altered (Figure S6, S7), which accounts for some of the detection location uncertainty.

508           Given these observations, it seems the  $b$  value is not a good indicator for when The  
509 Geysers might enter a ‘prepared’ state for triggering to occur or even where triggering is most  
510 likely to occur in the region. There is one possible explanation for  $b$  values being  
511 indistinguishable between triggered and non-triggered nodes in The Geysers. If the  $b$  value is an  
512 indicator of differential stress, then similar  $b$  values between triggered and non-triggered nodes  
513 would suggest that their differential stresses are also likely to be similar. It follows then that for a  
514 node to be triggered it probably has a lower mean stress (relative to a non-triggered node),  
515 placing it closer to failure [e.g., *Beeler*, 2000]. That is to say, a triggered and non-triggered node  
516 would experience similar dynamic stressing from a distant earthquake, but a node that has lower  
517 mean stress (greater pore fluid pressures) would have greater susceptibility to being triggered.

518           We note the  $b$  value (slope of the Gutenberg-Richter distribution) is highly dependent  
519 upon catalogued events -- detected by a seismic network and/or other methods. While we did not  
520 include matched filter detected events in our  $b$  value evaluation, the  $b$  value observations  
521 presented above should not be very different if these detections were included in the analysis.  
522 This is because the matched filter method increases the number of small magnitudes events,  
523 events that are often missed by seismic networks. Thus, if more small magnitude events were  
524 included in the  $b$  value evaluation, it would be expected that the  $b$  value should either remain the  
525 same or increase (Figure 2). Since a high  $b$  value is indicative of low differential stress, adding  
526 the matched filter detected events to the  $b$  value calculation would not significantly alter the  
527 conclusion that  $b$  values are not a good indicator of The Geysers entering a ‘prepared’ stress  
528 state.



529

530 **Figure 7. (a)** Triggered and non-triggered node  $b$  value calculations prior to all mainshocks.  
 531 Error as calculated in equation (4). **(b)** Same as (a) but for 100 randomly generated earthquake  
 532 samples at each node. Mean  $b$  values and mean error computed from randomly generated  
 533 catalogs are similar to the true distribution in (a), illustrating  $b$  value stability. **(c)** Normalized  
 534 probability distribution functions for triggered (black line) and non-triggered (gray line)  $b$  value  
 535 populations in (a), with both having means of 1.02. **(d)** Open circles:  $b$  values at each triggered  
 536 node and the number of events triggered in that node during the triggering time window. Black  
 537 circles: rolling mean  $b$  value.

538

## 539 6.2 Tidal stress changes

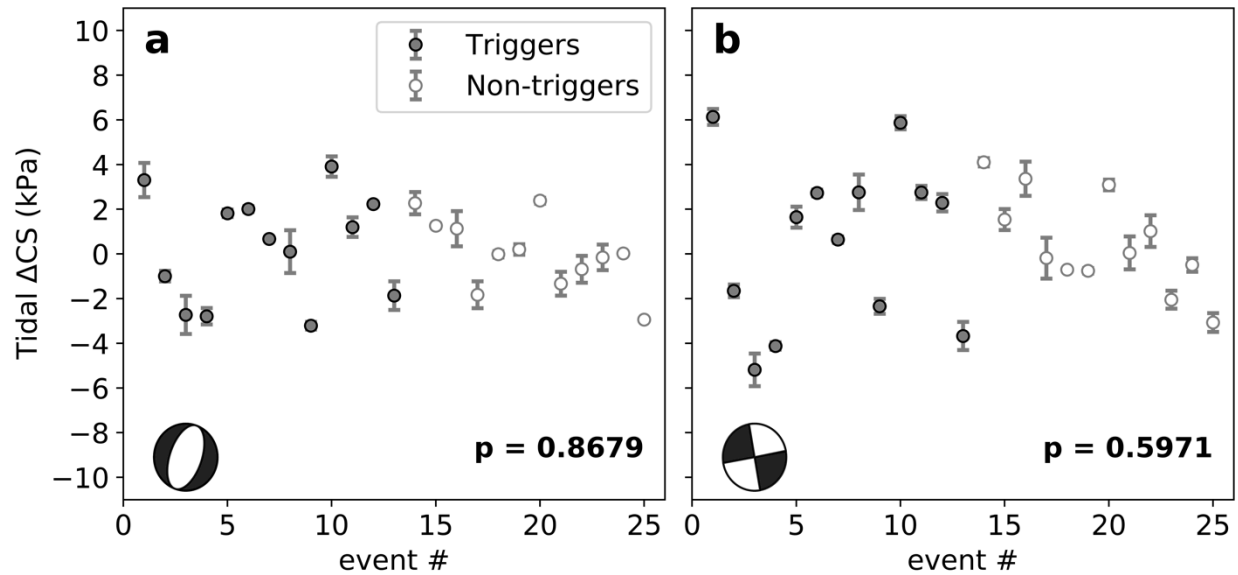
540 Tidal stresses from ocean and solid Earth tides can reach up to as much as 10 kPa, the  
 541 same order of magnitude for dynamic stresses generated by large mainshocks occurring at  
 542 remote distances (e.g., Figure 4c). Thus, tidal stresses could influence The Geysers response to  
 543 transient stresses generated by distant mainshocks, if the tidal stresses are significantly large  
 544 during the same time as the passing seismic waves. Some Programs for Ocean Tide Loading  
 545 (SPOTL) [Agnew, 1996] can predict tidal strains from gravitational forcing between the Sun,  
 546 Moon, and Earth as well as loading from changes in ocean tide height. We computed solid-earth

547 (body) tidal strains around the time of each mainshock using the *ertid* program within SPOTL  
548 and computed ocean tidal strains for the M2, N2, S2, K2, K1, O1, P1, and Q1 frequencies using  
549 the global TOPEX/POSEIDON model and a local USA west coast model within the SPOTL  
550 program. In all cases, we summed the strains for each frequency component and computed the  
551 Hookean stress histories of the tidal forcing in the first 2 hours since each mainshock's *P* wave  
552 arrival in The Geysers, since triggering starts some time during the passing of a mainshock's  
553 seismic waves. We assume the shallow crust is a Poisson solid with a shear modulus of 30 GPa,  
554 where the stresses act anisotropically in The Geysers' fluid-rich environment due to poroelastic  
555 effects. We resolved these stresses onto planes parallel to The Geysers two representative  
556 faulting styles we observed in this study – strike slip and normal faulting (Section 2). We then  
557 used the resolved normal and shear stress changes to compute the Coulomb stress changes ( $\Delta CS$ )  
558 due to tidal forcing on each fault type, such that

$$559 \quad \Delta CS = \Delta \tau + \mu(\Delta \sigma_n - \Delta p) \quad (5)$$

560 where  $\Delta \tau$  is shear stress change in the rake direction,  $\mu$  is the coefficient of friction,  $\Delta \sigma_n$  is the  
561 normal stress change, and  $\Delta p$  is pore pressure change. Here, we assume that  $\mu = 0.7$  and  $\Delta p = -$   
562  $B\sigma_{kk}/3$  where  $B$  is the Skempton coefficient ( $B = 0.7$ ) and  $\sigma_{kk}$  is the trace of the stress tensor  
563 rotated to the fault planes at each point in time.

564 Figure 8 illustrates the mean Coulomb stress changes ( $\Delta CS$ ) computed from the summed  
565 body and ocean tidal forces in the first 2 hours following triggering and non-triggering  
566 mainshocks. There is no difference in the magnitude of tidal stress changes when triggering  
567 occurs and when triggering does not occur for both the normal and strike-slip fault cases. Thus, it  
568 seems that tidal stress does not play a role in the timing of The Geysers' susceptibility to  
569 triggering.



570

571 **Figure 8.** Resolved Coulomb stress changes due to solid Earth (body) and ocean tidal forcing on  
 572 The Geysers representative (a) normal fault and (b) strike-slip fault during the first 2 hours  
 573 following the *P* wave arrival of the 25 mainshocks. As shown by the *p* values from Kolmogorov-  
 574 Smirnov tests, there is no difference between tidal stresses when triggering occurs ( $Z > 1.96$ ) and  
 575 when triggering does not occur ( $Z < 1.96$ ) for either fault type. Thus, tidal forcing does not seem  
 576 to have any effect on Geysers' susceptibility to triggering. Event # in this figure is the same as in  
 577 Figure 5a-d.

578

579

580 **7. Discussion**

581

582

583

584

585

586

587

588

589

Dynamic triggering has been identified in non-geothermal regions such as fluid-injection sites in the Central US [van der Elst et al., 2013], but The Geysers' is a unique site for testing the 'predictability' of dynamic triggering. Beyond having fluid mass fluctuations, it has been suggested The Geysers has a greater susceptibility to triggering based on its higher heat flow [Aiken and Peng, 2014] and background seismicity rate [Hill and Prejean, 2015]. However, it's possible that The Geysers' appears to be uniquely more susceptible because of its proximity to repeatable triggering sources coming from the MTJ. In this study, we discovered that there is some repeatability of triggering in The Geysers with mainshocks occurring in the MTJ of a certain size and orientation (Figures 1 and 6). The Geysers may, in the future, be repeatedly

590 triggered by more distant mainshocks (i.e. teleseisms). However, at teleseismic distances, larger  
591 magnitude mainshocks are required for triggering to be observed, and larger magnitude  
592 mainshocks are far less frequent than those occurring in the MTJ. Thus, more observation time is  
593 needed to test the repeatability of triggering by mainshocks at teleseismic distances.

594 We found that maximum magnitude of triggered events positively correlates with peak  
595 dynamic stress changes, and at larger dynamic stress changes ( $> 20$  kPa), the highest magnitude  
596 triggered event tends to occur earlier in the triggered sequence (Figure 4c). This suggests that  
597 larger dynamic stresses are more likely to encourage mainshock-aftershock type sequences, a  
598 phenomenon previously observed in The Geysers [*Brodsky, 2006*]. On the other hand, smaller  
599 peak dynamic stresses tend to trigger smaller magnitude events with the highest magnitude  
600 triggered event occurring much later in the sequence, suggesting more swarm-like behavior.  
601 Thus, we may be able to forecast the largest magnitude of the triggered sequence, and perhaps  
602 even how the triggering episode will evolve in time.

603 We considered the possibility that triggering might occur when The Geysers is in a high  
604 differential stress state, a preparatory stage for the release of stress in a triggering episode. While  
605 it has been shown (in retrospect) that the  $b$  value of the Gutenberg-Richter magnitude-frequency  
606 distribution could map high differential stress and an impending earthquake rupture area [e.g.,  
607 *Schorlemmer and Wiemer, 2005*], we found no significant difference between  $b$  values in  
608 triggered areas and non-triggered areas (Figure 7). Small magnitude earthquakes, like those in  
609 The Geysers' triggering episodes, occur regularly in The Geysers due to the on-going geothermal  
610 energy production, and thus there may not be a significant amount of time for stress build up that  
611 could be visible with a spatial  $b$ -value analysis. Moreover, since we observed similar  $b$  values in  
612 triggered and non-triggered nodes and The Geysers has mostly small magnitude ( $M < 4$ ) events,

613 we presume that highly variable fluid mass fluctuations for energy production may lower  
614 recurrence times by creating a highly fractured network of many nucleation points. This might  
615 break standard ideas about the distribution of earthquake behavior in time, such as the slope of  
616 the Gutenberg-Richter distribution ( $b$  value) prior to triggering. Hence, it remains unclear if  
617 small magnitude events can be used to understand local stress state.

618         It has been shown that tidal stresses from solid Earth tides and ocean loading can  
619 influence slow earthquake (a.k.a. tremor) activity [*Thomas et al.*, 2009; *Houston*, 2015], but we  
620 found no evidence that tidal stresses have any influence on when triggering happens in The  
621 Geysers (Figure 8). This counters recent observations that tidal forcing can influence earthquake  
622 activity in non-geothermal regions, a relationship that is highly dependent upon the magnitude of  
623 the tidal stress [*Bucholc and Steacy*, 2016]. The tidal stress changes we observed were at most  
624 +/- 6 kPa during the triggering time window, the same order of magnitude but still less than  
625 current triggering thresholds for geothermal areas of California [*Aiken and Peng*, 2014]. Yet, we  
626 observed no clear distinction between tidal stress changes during triggering and non-triggering  
627 mainshocks. Therefore, it remains unclear what role, if any, tidal stresses and local stresses may  
628 play in the triggering process.

629

## 630 **8. Conclusions**

631         At present, seismicity induced by geothermal energy production at The Geysers is not  
632 generally considered to pose a significant seismic hazard [e.g., *Majer et al.*, 2007]. However,  
633 based on this study, it appears that larger dynamic stress changes from distant mainshocks trigger  
634 larger events. Therefore, it is vital to understand when, where, and how triggering will occur for  
635 the safety of on-going energy operations at The Geysers, especially since moderate sized

636 earthquakes occurring in the Mendocino Triple Junction repeatedly trigger the region and occur  
637 more frequently than larger, more distant earthquakes. But how ‘predictable’ is dynamic  
638 triggering of earthquakes at The Geysers? With the few cases we investigated in this study, it is  
639 clear that at least the timing and location of triggering is not well understood.

640         The most difficult challenge in understanding the ‘predictability’ of dynamically  
641 triggered earthquakes is determining where the weak points are (when and where triggering is  
642 most likely to happen) and what controls those weaknesses. One likely factor that we did not  
643 investigate in this study is the role of fluid mass fluctuations. *Brodsky and Lajoie* [2013] showed  
644 that earthquake activity in Salton Sea geothermal field, at least, is closely tied to the total fluid  
645 volume. However, it was beyond the scope of this work to investigate whether or not fluid  
646 injection/extraction volumes in The Geysers heightens susceptibility to dynamic triggering.  
647 Since triggered earthquakes sometimes occur in isolated areas (Figure 4a), it may even be  
648 worthwhile to analyze fluid-injection volumes at individual wells and their relationships with  
649 earthquake activity [e.g., *Majer and Peterson, 2007; Langenbruch and Zoback, 2016*]. Such  
650 investigations would add some clarity to The Geysers’ stress state around the times triggering  
651 does and does not happen and where triggering might happen in the future.

652

## 653 **Data and Resources**

654 Waveform data, metadata, or data products for this study were accessed through the Northern  
655 California Earthquake Data Center (NCEDC), doi:10.7932/NCEDC. The ANSS catalog is a  
656 comprehensive catalog (a.k.a. ComCat) is accessible at [http://www.ncedc.org/anss/catalog-  
657 search.html](http://www.ncedc.org/anss/catalog-search.html) (last accessed July 27, 2017). The EGS catalog is a catalog developed by Lawrence  
658 Berkeley National Laboratory and is accessible at <http://www.ncedc.org/egs/catalog-search.html>  
659 (last accessed July 27, 2017). Phase arrival times were computed using the *TauP* program, freely  
660 available at <http://www.seis.sc.edu/TauP/>. Focal mechanisms of The Geysers’ earthquakes were  
661 computed using the HASH program, freely available at  
662 <https://earthquake.usgs.gov/research/software/#HASH>. Focal mechanisms of potentially

663 triggering mainshocks were taken from the openly available Harvard CMT catalog  
664 (<http://www.globalcmt.org/CMTsearch.html>, last accessed January 16, 2018).  
665 We assessed site geology for the GDXB station from the Center for Engineering Strong Motion  
666 Data ([http://www.strongmotioncenter.org/cgi-](http://www.strongmotioncenter.org/cgi-bin/CESMD/stationhtml.pl?stationID=NCGDXB&network=NCSN)  
667 [bin/CESMD/stationhtml.pl?stationID=NCGDXB&network=NCSN](http://www.strongmotioncenter.org/cgi-bin/CESMD/stationhtml.pl?stationID=NCGDXB&network=NCSN) , last accessed November  
668 17, 2017). Figures 1, 2, 4, and 5 were made using Python 3.3, an open source programming  
669 language.  
670

## 671 **Acknowledgements**

672 We thank Justin Rubinstein and Andrea Llenos for comments that improved an earlier draft of  
673 our manuscript. We also thank two anonymous reviewers for their time and helpful feedback that  
674 greatly improved the quality of our manuscript. UTIG contribution #3142.  
675

## 676 **References**

- 677 Agnew, D. C. (1996), SPOTL: Some programs for ocean-tide loading, *SIO Ref. Ser. 96-8*, 35 pp.,  
678 Scripps Institution of Oceanography, La Jolla, CA.  
679
- 680 Aki, K. (1965), Maximum likelihood estimate of b in the formula  $\log N = a - bM$  and its  
681 confidence limits, *Bull. Earthq. Res. Inst.*, 43, 237-239.  
682
- 683 Aiken, C. and Z. Peng (2014), Dynamic triggering of microearthquakes in three geothermal  
684 regions of California, *J. Geophys. Res.*, 119, 6992-7009, doi: 10.1002/2014JB011218.  
685
- 686 Aiken, C., Z. Peng, and K. Chao (2013), Tremors along the Queen Charlotte Margin triggered by  
687 large teleseismic earthquakes, *Geophys. Res. Lett.*, 40, doi:10.1002/grl.50220.  
688
- 689 Brodsky, E. E. (2006), Long-range triggered earthquakes that continue after the wave train  
690 passes, *Geophys. Res. Lett.*, 33, L15313, doi:10.1029/2006GL026605.  
691
- 692 Brodsky, E. E. and L. J. Lajoie (2013), Anthropogenic seismicity rates and operational  
693 parameters at the Salton Sea Geothermal Field, *Science*, 341, 543-546, doi:  
694 10.1126/science.1239213.  
695
- 696 Brodsky, E. E. and N. J. van der Elst (2014), The uses of dynamic earthquake triggering, *Annu.*  
697 *Rev. Earth Pl. Sc.*, 42, 317-339, doi: 10.1146/annualrev-earth-060313-054648.  
698
- 699 Boyle, K., and M. Zoback (2014), The Stress State of the Northwest Geysers, California  
700 Geothermal Field, and Implications for Fault-Controlled Fluid Flow, *Bull. Seismol. Soc. Am.*,  
701 doi: 10.1785/0120130284.  
702
- 703 Bucholc, M. and S. Steacy (2016), Tidal stress triggering of earthquakes in Southern California,  
704 *Geophys. J. Int.*, 205, no. 2, 681-693, doi: 10.1093/gji/ggw045.

705  
706 Dieterich, J. (1994), A constitutive law for rate of earthquake production and its application to  
707 earthquake clustering. *J. Geophys. Res.*, 99, B2, 2601–2618, doi:10.1029/93JB02581.  
708  
709 Felzer, K. and E. E. Brodsky (2006), Decay of aftershock density with distance indicates  
710 triggering by dynamic stress, *Nature*, 441, 735-738, doi: 10.1038/nature04799.  
711  
712 Goebel, T. H. W., D. Schorlemmer, T. W. Becker, G. Dresen, C. G. Sammis (2013), Acoustic  
713 emissions document stress changes over many seismic cycles in analog  
714 experiments, *Geophys. Res. Lett.*, 40, no. 10, 2049-2054, doi:10.1029/2013GL050507.  
715  
716 Gomberg, J. (2010), Lessons from (triggered) tremor, *J. Geophys. Res.*, 115, B10302, doi:  
717 10.1029/2009JB007011.  
718  
719 Gomberg, J. and Johnson, P. A. (2005), Dynamic triggering of earthquakes, *Nature* 473, 830,  
720 doi: 10.1038/437830a.  
721  
722 Gonzalez-Huizar, H. and A. A. Velasco (2011), Dynamic triggering: Stress modeling and a case  
723 study, *J. Geophys. Res.*, 116, B02304, doi: 10.1029/2009JB007000.  
724  
725 Habermann, R. E. (1981), Precursory seismicity patterns: Stalking the mature seismic gap, in  
726 Earthquake Prediction – An international review, ed. D. W. Simpson and P. G. Richards,  
727 pp. 29-42, *American Geophysical Union*.  
728  
729 Habermann, R. E. (1983), Teleseismic detection in the Aleutian Island Arc, *J. Geophys. Res.*,  
730 88, 5056-5064.  
731  
732 Hardebeck, J. L. (2014), The impact of static stress change, dynamic stress change, and the  
733 background stress on aftershock focal mechanisms, *J. Geophys. Res.*, 119, no. 11, 8239-  
734 8266, doi: 10.1002/2014JB011533.  
735  
736 Hardebeck, J. L. and P. M. Shearer (2002), A new method for determining first-motion focal  
737 mechanisms, *B. Seismol. Soc. Am.*, 92, no. 6, 2264-2276.  
738  
739 Hawkins, A., D. L. Turcotte, M. B. Yikilmaz, L. H. Kellog, and J. B. Bundle (2017), Statistical  
740 studies of induced and triggered seismicity at The Geysers, California, *Pure Appl. Geophys.*,  
741 174, no. 6, 2443-2456, doi: 10.1007/s00024-017-1569-z.  
742  
743 Hill, D. P. (2012), Surface wave potential for triggering tectonic (non-volcanic) tremor --  
744 Corrected, *B. Seismol. Soc. Am.*, 102, no. 6, 2313-2336, doi:10.1785/0120120085.  
745  
746 Hill, D. P. (2015), On the sensitivity of transtensional versus transpressional tectonic regimes to  
747 remote dynamic triggering by Coulomb failure, *B. Seismol. Soc. Am.*, 105, no. 3,  
748 doi:10.1785/0120140292.  
749  
750 Hill, D. P., et al. (1993), Seismicity remotely triggered by the magnitude 7.3 Landers, California,

751 earthquake, *Science*, 260(5114), 1617–1623.  
752  
753 Hill, D. P. and S. G. Prejean (2015), Dynamic Triggering, in *Treatise on Geophysics* 2<sup>nd</sup> edition  
754 (G. Schubert, ed.), Chapter 8 in Volume 4, “Earthquake Seismology” (H. Kanamori, ed.),  
755 Elsevier, Amsterdam.  
756  
757 Houston, H. (2015), Low friction and fault weakening revealed by rising sensitivity of tremor to  
758 tidal stress, *Nat. Geosci.*, 8, 409-415, doi: 10.1038/ngeo2419.  
759  
760 King, G. C. P., R. S. Stein, and J. Lin (1994), Static stress changes and the triggering of  
761 earthquakes, *B. Seismol. Soc. Am.*, 84, no. 3, 935-953.  
762  
763 Langenbruch, C. and M. D. Zoback (2016), How will induced seismicity in Oklahoma respond  
764 to decreased saltwater injection rates?, *Science Advances*, 2, no. 11, e1601542, doi:  
765 10.1126/sciadv.1601542.  
766  
767 Majer, E. L. and J. E. Peterson (2007), The impact of injection on seismicity at The Geysers,  
768 California Geothermal Field, *Int. J. Rock Mech. Min.*, 44, no. 8, 1079-1090, doi:  
769 10.1016/j.ijrmms.2007.07.023.  
770  
771 Marsan, D. and M. Wyss (2011), Seismicity rate changes, Community Online Resource for  
772 Statistical Seismicity Analysis, doi: 10.5078/corssa-25837590. Available at  
773 <http://www.corssa.org>.  
774  
775 Martínez-Garzon, P., M. Bohnhoff, G. Kwiatek, and G. Dresen (2013), Stress tensor changes  
776 related to fluid injection at The Geysers geothermal field, California, *Geophys. Res. Lett.*, 40,  
777 no. 11, 2596-2601, doi: 10.1002/grl.50438.  
778  
779 Marzocchi, W. and L. Sandri (2003), A review and new insights on the estimation of the *b*-value  
780 and its uncertainty, *Ann. Geophys. Italy*, 46, no. 6, 1271 – 1282.  
781  
782 Meng, X., Z. Peng, and J. Hardebeck (2013), Seismicity around Parkfield correlates with static  
783 shear stress changes following the 2003 Mw6.5 San Simeon earthquake, *J. Geophys. Res.*,  
784 118, no. 7, 3576-3591, doi: 10.1002/jgrb.50271.  
785  
786 Mignan, A., J. Woessner (2012), Estimating the magnitude of completeness for earthquake  
787 catalogs, Community Online Resource for Statistical Seismicity Analysis,  
788 doi:10.5078/corssa-00180805. Available at <http://www.corssa.org>.  
789  
790 Nava, F. A., V. H. Márquez-Ramírez, F. R. Zúñiga, L. Ávila-Barrientos, C. B. Quinteros (2017),  
791 Gutenberg-Richter *b*-value maximum likelihood estimation and sample size, *J. Seismol.*, 21,  
792 no. 1, 127-135, doi: 10.1007/s10950-016-9589-1.  
793  
794 Peng, Z., J. Walter, R. Aster, A. Nyblade, D. Wiens, and S. Anandakrishnan (2014), Antarctic  
795 icequakes triggered by the 2010 Maule earthquake in Chile, *Nat. Geosci.*, 7, 677-681, doi:  
796 10.1038/NGEO2212.

797  
798 Peng, Z., and P. Zhao (2009), Migration of early aftershocks following the 2004 Parkfield  
799 earthquake, *Nat. Geosci.*, 2(12), 877–881.  
800  
801 Prejean, S. G., D. P. Hill, E. E. Brodsky, S. E. Hough, M. J. S. Johnston, S. D. Malone, D. H.  
802 Oppenheimer, A. M. Pitt, and K. B. Richards-Dinger (2004), Remotely triggered seismicity  
803 on the United States west coast following the *M<sub>w</sub>7.9* Denali Fault earthquake, *B. Seismol.*  
804 *Soc. Am.*, 94, No. 6B, S348-S359, doi: 10.1785/0120040610.  
805  
806 Pollitz, F. F. (1996), Coseismic deformation from earthquake faulting on a layered spherical  
807 Earth, *Geophys. J. Int.*, 125, no. 1, 1-14, doi: 10.1111/j.1365-246X.1996.tb06530.x.  
808  
809 Schaff, D. P. and P. G. Richards (2014), Improvements in magnitude precision, using the  
810 statistics of relative amplitudes measured by cross correlation, *Geophys. J. Int.*, 197, no. 1,  
811 335-350, doi: 10.1093/gji/ggt433.  
812  
813 Schorlemmer, D., G. Neri, S. Wiemer, and A. Mostaccio (2003), Stability and significance tests  
814 for *b*-value anomalies: Example from the Tyrrhenian Sea, *Geophys. Res. Lett.*, 30, no. 16,  
815 doi: 10.1029/2003GL017335.  
816  
817 Schorlemmer, D. and S. Wiemer (2005), Microseismicity data forecast rupture area, *Nature*, 434,  
818 1086.  
819  
820 Shelly, D., G. Beroza, and S. Ide (2007), Non-volcanic tremor and low-frequency earthquake  
821 swarms, *Nature*, 446(7133), 305–307.  
822  
823 Shi, Y. and B. A. Bolt (1982), The standard error of the magnitude-frequency *b* value, *B.*  
824 *Seismol. Soc. Am.*, 72, no. 5, 1677-1687.  
825  
826 Tormann, T., S. Wiemer, and A. Mignan (2014), Systematic survey of high-resolution *b* value  
827 imaging along Californian faults: Inference on asperities, *J. Geophys. Res.*, 119, no. 3, 2029-  
828 2054, doi: 10.1002/2013JB010867.  
829  
830 Thomas, A., R. M. Nadeau, and R. Bürgmann (2009), Tremor-tide correlations and near-  
831 lithostatic pore pressure on the deep San Andreas fault, *Nature*, 462, 1048-1051, doi:  
832 10.1038/nature08654.  
833  
834 van der Elst, N. J., H. M. Savage, K. M. Keranen, and G. A. Abers (2013), Enhanced remote  
835 earthquake triggering at fluid-injection sites in the Midwestern United States, *Science*, 341,  
836 164-167, doi: 10.1126/science.1238948.  
837  
838 Wiemer, S., and M. Wyss (2000). Minimum magnitude of complete reporting in earthquake  
839 catalogs: examples from Alaska, the Western United States, and Japan, *Bull. Seismol. Soc.*  
840 *Am.*, 90, 859–869.  
841

842 Ziv, A., A. M. Rubin, and D. Kilb (2003), Spatiotemporal analyses of earthquake productivity  
843 and size distribution: Observations and simulations, *B. Seismol. Soc. Am.*, 93, no. 5, 2069-  
844 2081, doi: 10.1785/0120020117.

**Testing for the ‘predictability’ of dynamically triggered earthquakes in The Geysers geothermal field**

*Authored by*

Chastity Aiken, Xiaofeng Meng, and Jeanne Hardebeck

**1. Introduction**

This supplementary text contains the supplemental text, 9 supplementary figures and 2 supplementary tables.

**2. Supplemental Text**

**2.1 Combining ANSS/ComCat and EGS catalogs**

As seen in Figure 2 of the main text, the EGS earthquake catalog (see Data and Resources) is more complete than the ANSS/ComCat catalog. However, it only reports from 2003 to present. Since our potential triggering earthquake selection time period begins in 2001, we combine the ANSS/ComCat and EGS catalogs.

The EGS catalog reports local magnitudes ( $M_L$ ), while ANSS/ComCat reports a variety of magnitudes -- mostly  $M_d$  (duration magnitude) -- but also a few  $M_L$  and  $M_x$  (‘x’ possibly meaning average?) for The Geysers. Events with very similar origin times and locations appear in both the ANSS/ComCat and EGS catalogs but with different magnitudes and magnitude types. Since the Gutenberg-Richter  $b$  value (see Section 6.1 of main text) is dependent upon magnitude, it is important that similar magnitude types are used in the analysis.

To convert EGS  $M_L$  reported magnitudes to  $M_d$  magnitudes, we first determine events that are commonly reported in both the ANSS/ComCat and EGS catalogs. We define common reported events between the catalogs as having an origin time < 1 second and a separation distance < 1 km. We keep only ANSS/ComCat events that have magnitude type  $M_d$  and EGS events with magnitude  $M_L$ . We plot ANSS reported magnitude ( $M_d$ ) vs. EGS reported magnitude ( $M_L$ ) and perform a linear regression on the data (Figure S5). We find that to convert EGS reported magnitude ( $M_L$ ) to  $M_d$  we must use the following formula:

$$M_{ANSS} = M_{EGS} - 0.66$$

which is similar to the results of *Hawkins et al.* [2017].

**3. Supplemental Figures**

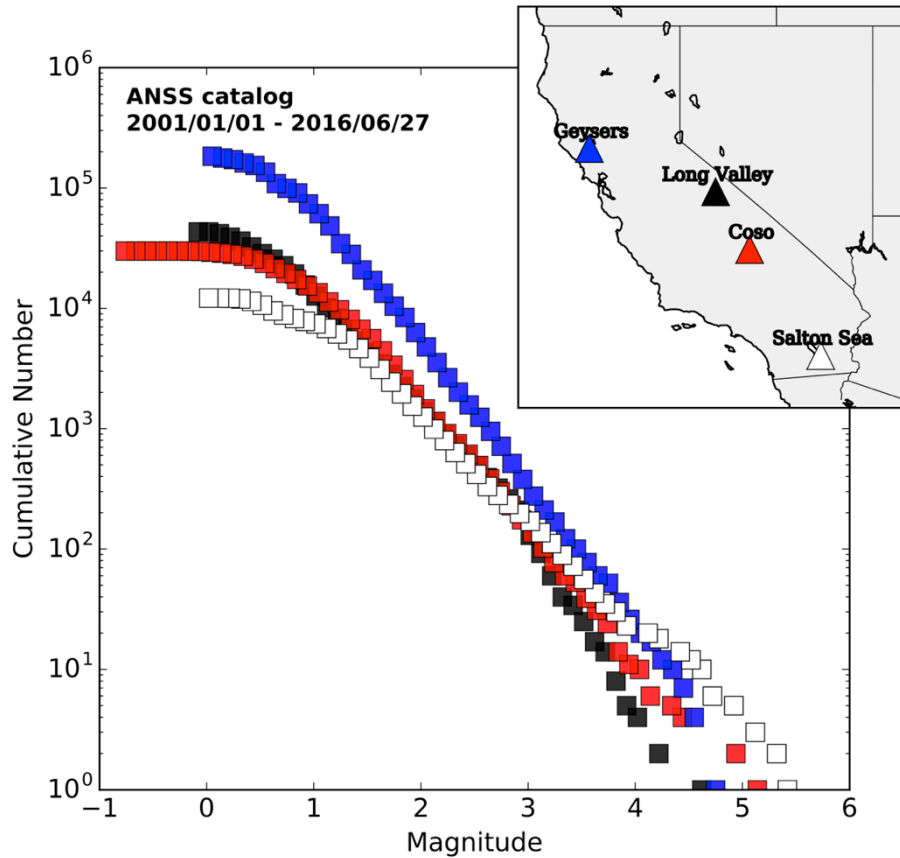


**Figure S1.** Over the last 15 years, The Geysers geothermal field has been the most seismically active geothermal region in California – more so than Long Valley Caldera, Coso geothermal field, and Salton Sea geothermal field combined, even when considering only events with  $M \geq 2$ . Geysers had 6305 earthquakes with  $M \geq 2$ , while Long Valley Caldera, Coso Geothermal Field, and Salton Sea Geothermal Field had 1541, 1924, and 1762 events, respectively. Only shallow ( $< 10$  km) events within a  $0.4^\circ \times 0.4^\circ$  area (colored squares) are shown as reported by the Advanced National Seismic System. The Geysers geothermal field (longitude min/max:  $123^\circ\text{W}$ ,  $122.6^\circ\text{W}$ ; latitude min/max:  $38.6^\circ\text{N}$ ,  $39^\circ\text{N}$ ); Long Valley (longitude min/max:  $119.1^\circ\text{W}$ ,  $118.7^\circ\text{W}$ ; latitude min/max:  $37.45^\circ\text{N}$ ,  $37.85^\circ\text{N}$ ); Coso geothermal field (longitude min/max:  $118.05^\circ\text{W}$ ,  $117.65^\circ\text{W}$ ; latitude min/max:  $35.9^\circ\text{N}$ ,  $36.3^\circ\text{N}$ ); Salton Sea geothermal field (longitude min/max:  $115.86^\circ\text{W}$ ,  $115.46^\circ\text{W}$ ; latitude min/max:  $33^\circ\text{N}$ ,  $33.4^\circ\text{N}$ )

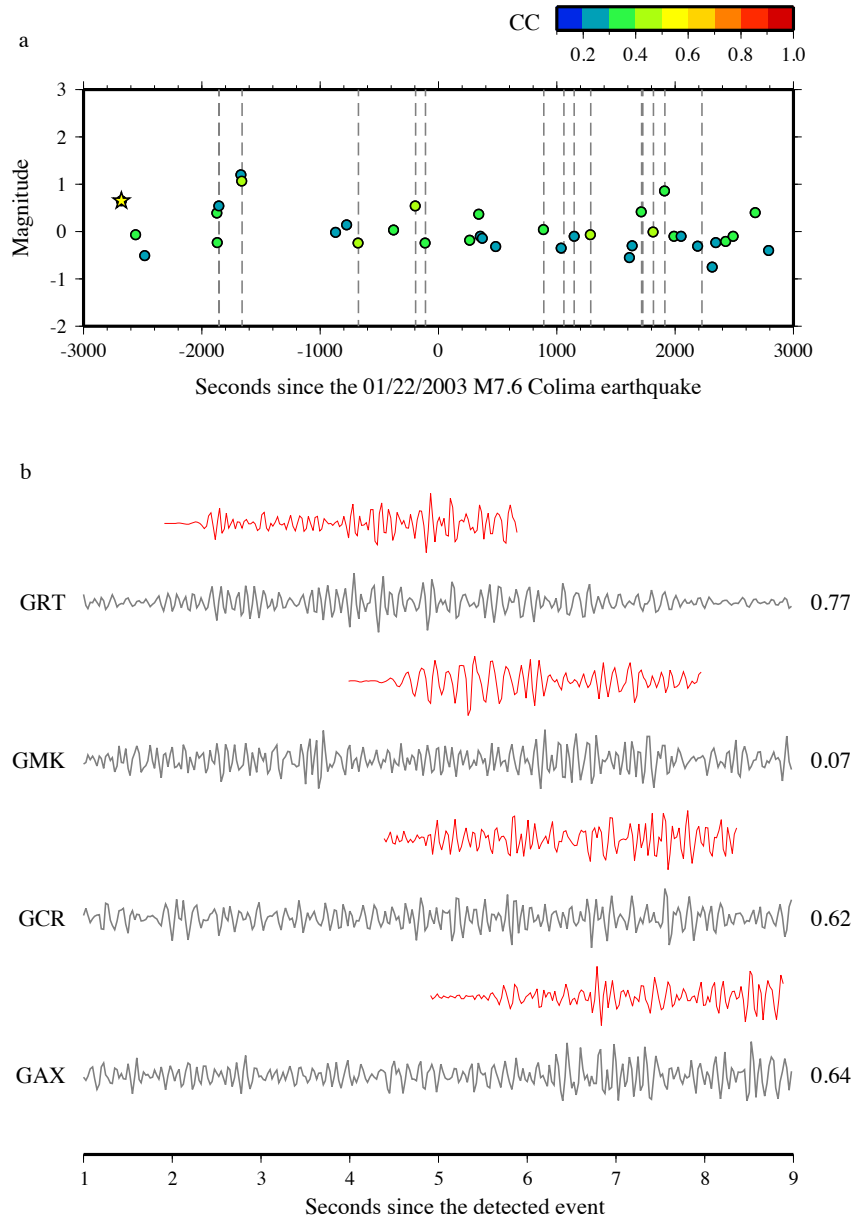


**Figure S2.** Example of small magnitude microearthquake detection. **(a)** Magnitude of microearthquakes detected around the time of the 01/22/2003 M7.6 Colima earthquake. Color indicates mean cross-correlation value from matched filter analysis. Gray dashed lines are times of events hand-picked by *Aiken and Peng* [2014]. **(b)** Gray and red waveforms are the continuous and template waveforms, respectively, for starred detected event in part (a). Station names are listed to the left of each continuous waveform. Cross-correlation values at each station are indicated on the right.

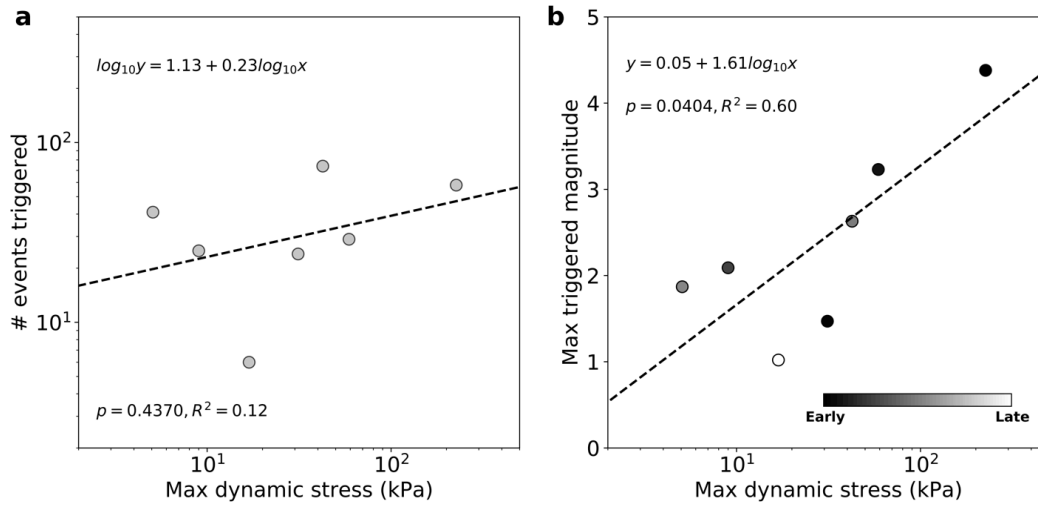


**Figure S3.** Same as Figure 2b and 2c, except when using matched filter catalogs made with a 12 x median absolute deviation threshold.

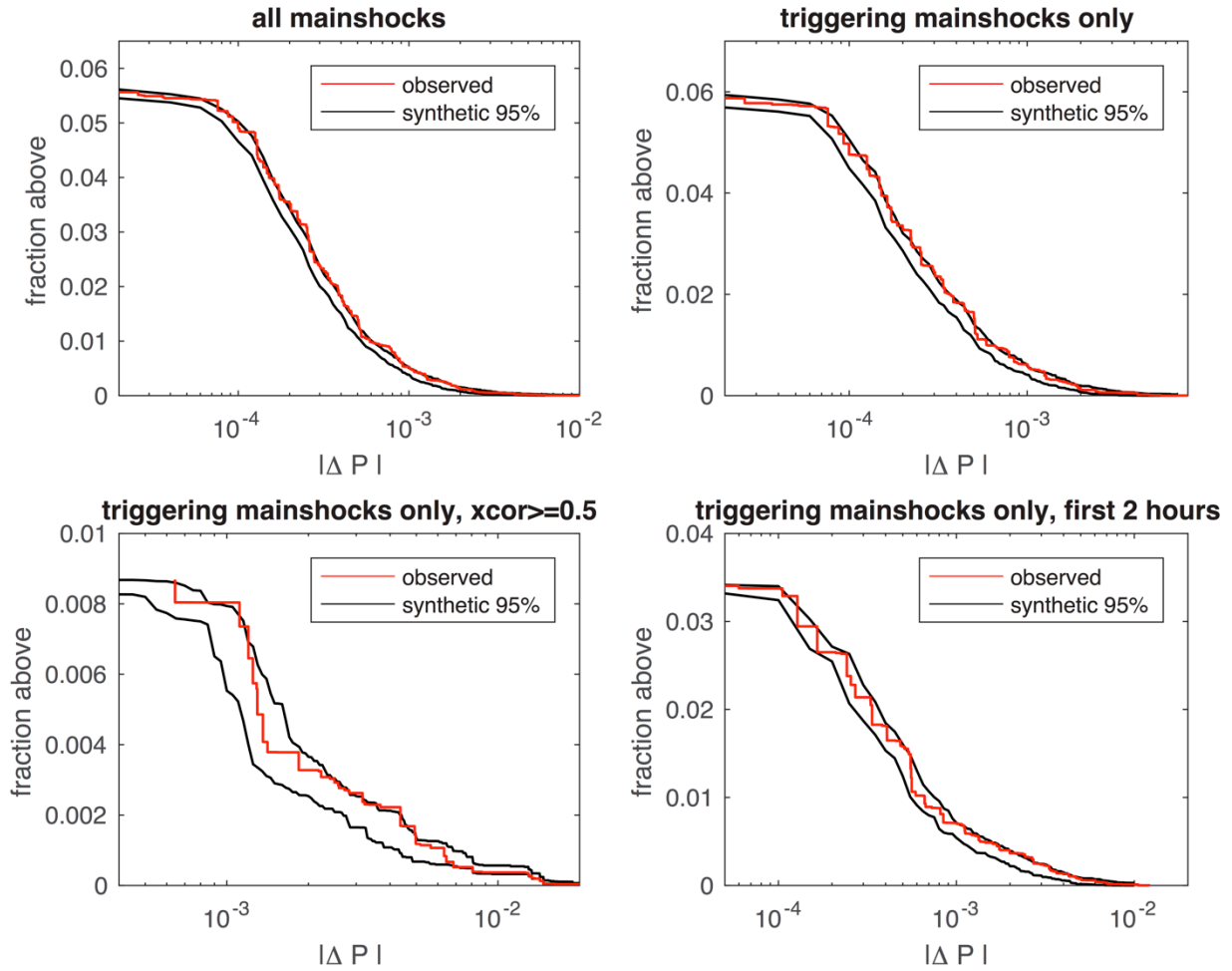


**Figure S4.** The change in the distribution of focal mechanisms before and after each mainshock, characterized as a joint PDF,  $P(\theta, \phi, \lambda)$ , of the trend and plunge ( $\theta$ ,  $\phi$ ) of the normal to the nodal plane, and the corresponding rake,  $\lambda$ . The distribution change is expressed as  $|\Delta P| = |P_{\text{post}} - P_{\text{pre}}|$ . The red curve shows the survival function of  $|\Delta P|$  for the observed events, while the black curves show the middle 95% of 1000 realization of reshuffling the data for each mainshock. The random reshufflings are meant to capture the values of  $\Delta P$  that can occur simply due to random chance, due to errors or unrelated fluctuations in the focal mechanism catalog. For each realization, we randomly assign events to the “pre-mainshock” and “post-mainshock” sets, retaining the original number of events in each set. We compute  $|\Delta P|$  for each realization in the same way it is computed for the real data. The fractions are small because  $|\Delta P| = 0$  for most  $(\theta, \phi, \lambda)$ . **(a)** A stack of results for all mainshocks. **(b)** A stack for the significantly triggering mainshocks, those with  $Z \geq 1.96$ . **(c)** A stack for the significantly triggering mainshocks, including only detected events with cross-correlation values ( $\text{xcor}$ )  $\geq 0.5$ . **(d)** A stack for the significantly triggering mainshocks, including only post-mainshock events within the first 2 hours.

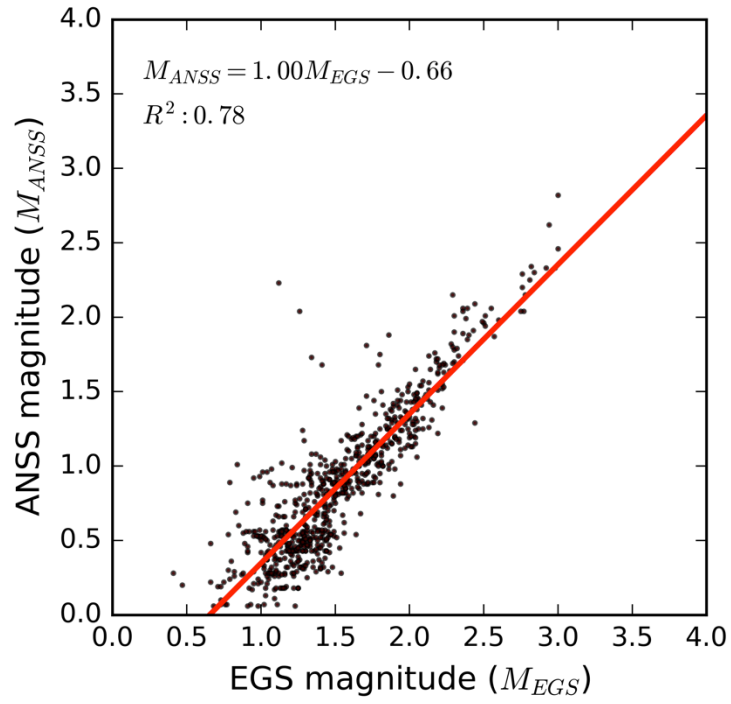


**Figure S5.** Linear regression fit for adjusting EGS magnitudes to ANSS magnitude scale.

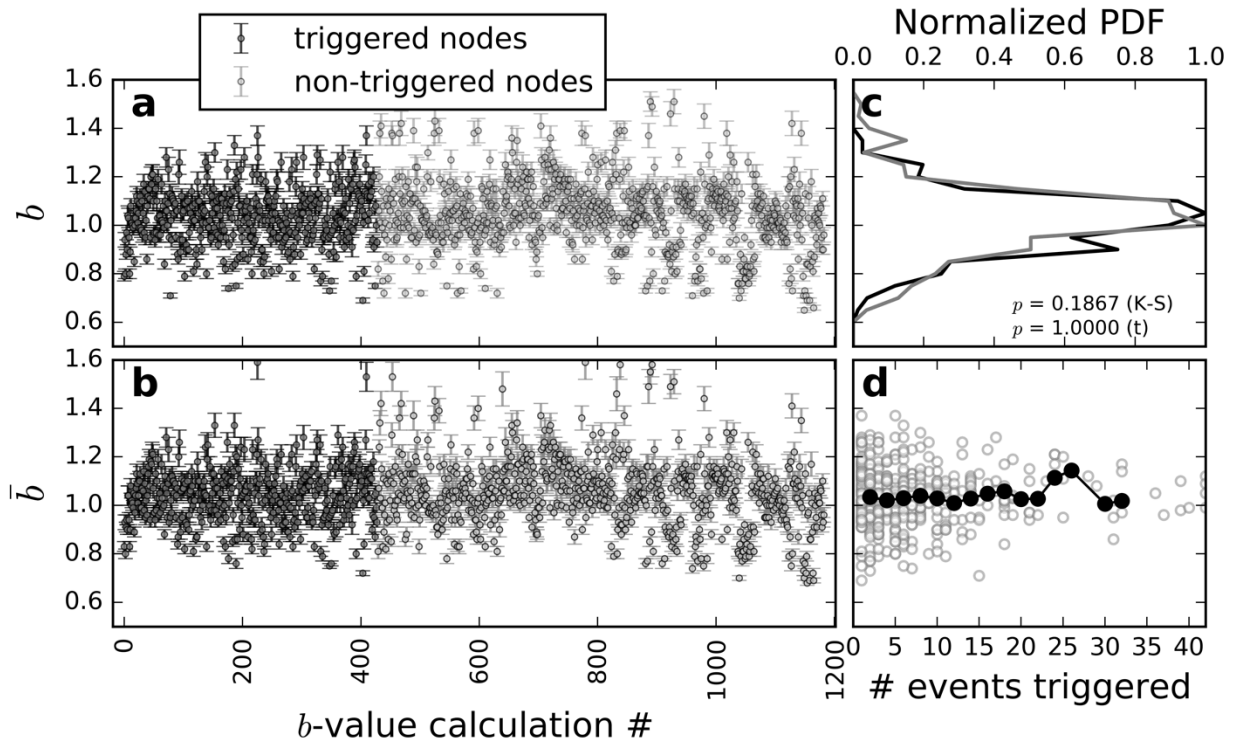


Figure S6. Same as Figure 7 but for  $0.02^\circ$  node spacing.

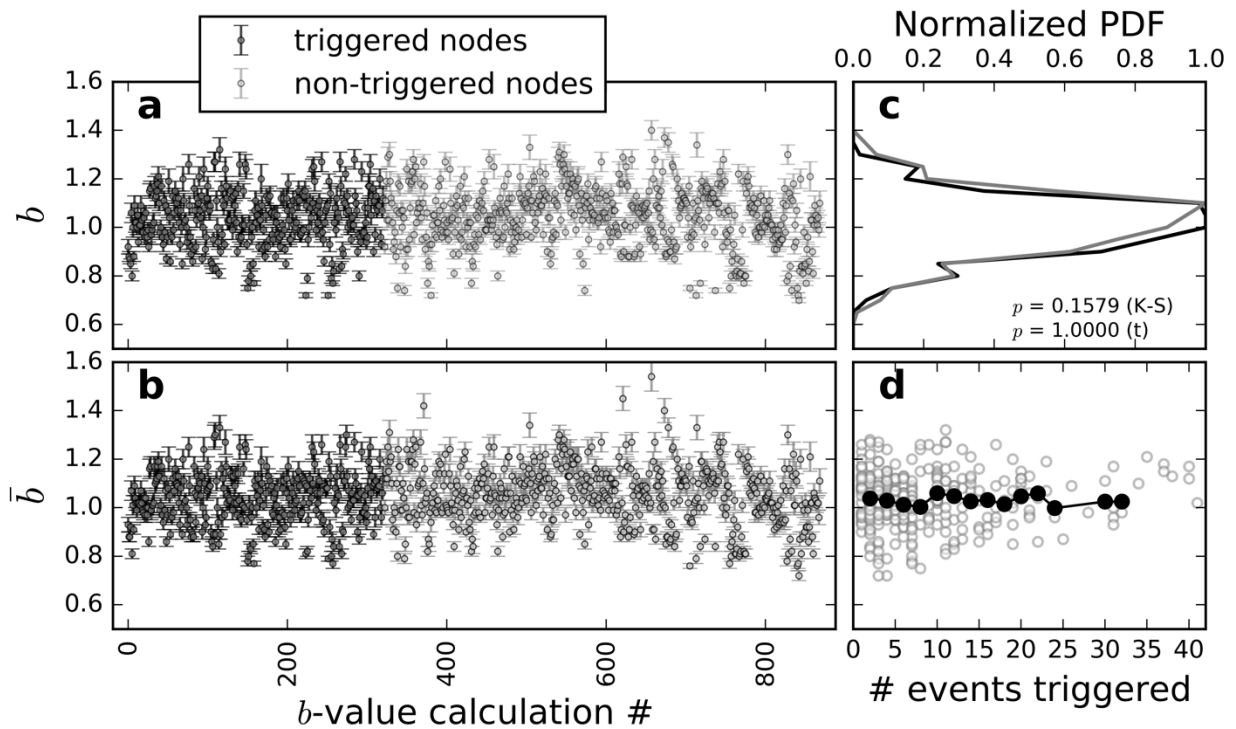


Figure S7. Same as Figure 7 but for  $0.03^\circ$  node spacing.

#### 4. Supplemental Tables

**Table S1. Seismic stations used for matched filter detection.**

<b>Network</b>	<b>Station</b>	<b>Channels</b>	<b>Location</b>
NC	GAC	EHZ	-122.8629, 38.8727
NC	GAX/GAXB	EHZ	-122.7573, 38.7107
NC	GBG	EHZ	-122.6826, 38.8144
NC	GCR	EHZ	-122.7172, 38.7733
NC	GDX	EHZ	-122.7953, 38.8080
NC	GGP/GGPB	EHZ	-122.8449, 38.7646
NC	GMK	EHZ	-122.7877, 38.9696
NC	GPM	EHZ	-122.9464, 38.8450
NC	GRT	EHZ	-122.6711, 38.9387
NC	GSG	EHZ	-122.7088, 38.8663
NC	NHS	EHZ	-122.6144, 38.6565
NC	NMC	EHZ	-122.9129, 38.5910
NC	NMH	EHZ	-122.6332, 38.6694
NC	NMW	EHZ	-122.7232, 38.5504
NC	NSH	EHZ	-122.6082, 38.5199

**Table S2. Template selection times by mainshock.**

<b>Date</b>	<b>Time</b>	<b>Region</b>	<b><math>M^*</math></b>	<b>Template Selection Window</b>	<b>Time</b>
1/13/2001	13:08:42	offshore CA	5.4	07/31/2000 – 07/13/2001	
9/20/2001	8:02:23	offshore CA	5.1	04/05/2001 – 02/12/2002	
6/23/2001	20:33:14	southern Peru	8.1	12/23/2000 – 11/28/2001	
6/17/2002	16:55:08	offshore CA	5.2	03/05/2002 – 09/29/2002	
11/3/2002	22:12:42	Denali, AK	7.9	07/30/2002 – 03/26/2003	
1/22/2003	2:06:35	Colima, MX	7.6	09/20/2002 – 05/23/2003	
8/15/2003	9:22:15	offshore CA	5.3	05/17/2003 – 12/20/2003	
6/15/2005	2:50:54	offshore CA	7.2	05/12/2005 – 07/21/2005	
1/4/2006	8:32:32	Gulf of CA	6.6	11/01/2005 – 03/08/2006	
7/19/2006	11:41:43	offshore CA	5.0	06/19/2006 – 09/01/2006	
1/13/2007	4:23:21	Kuril Islands	8.1	11/02/2006 – 05/04/2007	
2/26/2007	12:19:55	offshore CA	5.4	11/17/2006 - 06/15/2007	
5/9/2007	7:50:04	offshore CA	5.2	01/18/2007 – 08/10/2007	
6/25/2007	2:32:25	offshore CA	5.0	03/05/2007 – 09/09/2007	
4/30/2008	3:03:07	offshore CA	5.4	03/17/2008 – 06/30/2008	
8/3/2009	17:59:56	Baja CA	6.9	06/07/2009 – 10/07/2009	
1/10/2010	0:27:39	offshore CA	6.5	11/29/2009 – 02/17/2010	
2/4/2010	20:20:22	offshore CA	5.9	12/26/2009 – 03/08/2010	
2/27/2010	6:34:12	Maule, Chile	8.8	01/27/2010 – 04/01/2010	
4/4/2010	22:40:42	Baja CA	7.2	03/02/2010 – 05/07/2010	
2/13/2012	21:07:03	offshore CA	5.6	01/24/2012 – 03/07/2012	
7/21/2012	1:52:02	offshore CA	5.1	06/16/2012 – 08/30/2012	
3/10/2014	5:18:13	offshore CA	6.8	02/09/2014 – 04/10/2014	
8/24/2014	10:20:44	Napa, CA	6.0	07/18/2014 – 10/07/2014	
1/1/2015	12:16:15	offshore CA	5.3	11/27/2014 – 02/07/2015	
1/28/15	21:08:54	offshore CA	5.7	12/23/2014 - 02/26/2015	

\*Magnitude as listed in the ANSS/ComCat catalog.

**Table S3. Z value comparison for varied detection threshold**

<b>Mainshock Origin Time</b>	<b>Z, 9xMAD*</b>	<b>Z, 12xMAD*</b>
06/23/2001 20:33:14	<b>7.3</b>	<b>6.0</b>
09/20/2001 08:02:23	n/a	n/a
06/17/2002 16:55:08	<b>2.6</b>	n/a
11/03/2002 22:12:42	<b>11.5</b>	<b>8.5</b>
01/22/2003 02:06:35	<b>2.4</b>	n/a
08/15/2003 09:22:15	1.3	n/a
06/15/2005 02:50:54	<b>3.9</b>	1.6
01/04/2006 08:32:32	1.1	n/a
07/19/2006 11:41:43	0.5	n/a
01/13/2007 04:23:21	<b>2.3</b>	1.3
02/26/2007 12:19:55	1.7	n/a
05/09/2007 07:50:04	1.2	n/a
06/25/2007 02:32:25	<b>2.1</b>	n/a
04/30/2008 03:03:07	n/a	n/a
08/03/2009 17:59:56	<b>4.7</b>	<b>3.8</b>
01/10/2010 00:27:39	<b>2.7</b>	<b>2.3</b>
02/04/2010 20:20:22	0.9	n/a
02/27/2010 06:34:12	<b>4.6</b>	<b>4.8</b>
04/04/2010 22:40:42	<b>6.8</b>	<b>5.0</b>
02/13/2012 21:07:03	1.2	1.0
07/21/2012 01:52:02	-5.6	0.2
03/10/2014 05:18:13	<b>3.9</b>	1.2
08/24/2014 10:20:44	<b>10.4</b>	<b>7.2</b>
01/01/2015 12:16:15	1.0	n/a
01/28/2015 21:08:54	n/a	n/a

\*MAD = median absolute deviation